

CHANDRA OBSERVATIONS OF DIFFUSE GAS AND LUMINOUS X-RAY SOURCES AROUND THE X-RAY BRIGHT ELLIPTICAL NGC 1600

GREGORY R. SIVAKOFF, CRAIG L. SARAZIN, JEFFREY L. CARLIN

Department of Astronomy, University of Virginia, P. O. Box 3818, Charlottesville, VA 22903-0818

(Received 2004 May 24; Accepted 2004 Aug 19)

Astrophysical Journal, accepted

ABSTRACT

We observed the X-ray bright E3 galaxy NGC 1600 and nearby members of the NGC 1600 group with the *Chandra X-ray Observatory* ACIS S3 to study their X-ray properties. Unresolved emission dominates the observation; however, we resolved some of the emission into 71 sources, most of which are low-mass X-ray binaries (LMXBs) associated with NGC 1600. Twenty-one of the sources have $L_X > 2 \times 10^{39}$ ergs s⁻¹ (0.3–10.0 keV; assuming they are at the distance of NGC 1600) marking them as ultraluminous X-ray point source (ULX) candidates; we expect that only 11 ± 2 are unrelated foreground/background sources. NGC 1600 may have the largest number of ULX candidates in an early-type galaxy to date; however, cosmic variance in the number of background AGN cannot be ruled out. The spectra and luminosity function (LF) of the resolved sources are more consistent with sources found in other early-type galaxies than sources found in star-forming regions of galaxies. The source LF and the spectrum of the unresolved emission both indicate that there are a large number of unresolved point sources. We propose that these sources are associated with globular clusters (GCs), and that NGC 1600 has a large GC specific frequency. Observations of the GC population in NGC 1600 would be very useful to test this prediction. Approximately 50–75% of the unresolved flux comes from diffuse gaseous emission. The spectral fits, hardness ratios, and X-ray surface brightness profile all point to two gas components. We interpret the soft inner component ($a \lesssim 25''$, $kT \sim 0.85$ keV) as the interstellar medium of NGC 1600 and the hotter outer component ($a \gtrsim 25''$, $kT \sim 1.5$ keV) as the intragroup medium of the NGC 1600 group. The X-ray image shows several interesting structures. First, there is a central region of excess emission which is roughly cospatial with H α and dust filaments immediately west of the center of NGC 1600. There appear to be holes in the X-ray emission to the north and south of the galaxy center which are roughly coincident with the lobes of the NGC 1600 radio source. On larger scales, there is excess emission to the northeast, which we suggest may indicate the center of the group potential. The group galaxy NGC 1603 shows a tail of X-ray emission to its west which is probably due to ram-pressure stripping.

Subject headings: galaxies: elliptical and lenticular — galaxies: ISM — intergalactic medium — X-rays: binaries — X-rays: galaxies — X-rays: ISM

1. INTRODUCTION

X-ray emission in early-type galaxies generally comes from two sources, hot ($kT \sim 1$ keV) interstellar gas, and hard X-ray point sources whose properties are consistent with low-mass X-ray binaries (LMXBs). X-ray bright galaxies (those with relatively high L_X/L_B ratios, where L_X is X-ray luminosity and L_B is blue optical luminosity) are dominated by the interstellar gas (e.g., Forman, Jones, & Tucker 1985; Trinchieri, Fabbiano, & Canizares 1986), while X-ray faint galaxies (low L_X/L_B) have a large proportion of emission by LMXBs (Fabbiano, Kim, & Trinchieri 1994; Pellegrini 1994; Kim et al. 1996; Sarazin, Irwin, & Bregman 2000).

Since Fabbiano (1989), we have known that some of the off-nuclear X-ray point sources in spiral and elliptical galaxies have luminosities significantly exceeding the Eddington limit for $1 M_\odot$. These ultra-luminous X-ray point sources (ULXs) appear to occur preferentially in star-forming regions, (e.g., the Antennae: Zezas & Fabbiano 2002); however, early-type galaxies also contain bright point sources (e.g., NGC 1399 Angelini, Loewenstein, & Mushotzky 2001). In early-

type galaxies, there appear to be X-ray point sources with $L_X < 2 \times 10^{39}$ erg s⁻¹, consistent with accreting objects with masses $\lesssim 15 M_\odot$ (Irwin, Bregman, & Athey 2004). This mass limit is in line with current estimates of the upper mass limit of stellar mass black holes for progenitor masses $\lesssim 40 M_\odot$ (Fryer & Kalogera 2001). Above 2×10^{39} erg s⁻¹, the number of sources in previously observed early-type galaxies may be consistent with the number of expected background sources (Irwin et al. 2004). For this reason, we will adopt $L_X = 2 \times 10^{39}$ erg s⁻¹ as our minimum luminosity for a ULX candidate. Although the fainter ULXs could be explained by steady, spherically-symmetric, Eddington-limited accretion onto stellar-mass black holes, some other mechanism is required for the brighter ULXs.

ASCA results have indicated that the total luminosity of LMXBs in early-type galaxies correlates better with the number of globular clusters (GCs) than the optical luminosity of the galaxy (White, Sarazin, & Kulkarni 2002). *Chandra* observations of early-type galaxies have also shown that a significant fraction (20%–70%) of the LMXBs are associated with globular clusters in the host galaxies (Sarazin, Irwin, & Bregman 2000, 2001; Angelini et al. 2001; Kundu et al. 2003; Sarazin et al. 2003). It has been suggested that most, if not all,

of the LMXBs were formed in GCs (Grindlay 1984; Sarazin et al. 2000; White et al. 2002), and thus LMXBs can be used as tracers for GCs.

In this paper, we discuss *Chandra* observations of NGC 1600, an X-ray bright E3 galaxy. NGC 1600 is the brightest member of the NGC 1600 group; NGC 1601 (1.6' away) and NGC 1603 (2.5' away) are the two nearest galaxies, both of which are non-interacting members (de Vaucouleurs et al. 1992). We adopted the distance to NGC 1600 of 59.98 Mpc from Prugniel & Simien (1996), which assumes $H_0 = 75 \text{ km s}^{-1} \text{ Mpc}^{-1}$ and uses the Faber & Burstein (1988) model that accounts for the Virgocentric flow and the Great Attractor. NGC 1600 is a boxy elliptical with a radially anisotropic, axisymmetric three-integral distribution function. Combined with its lack of significant rotation, its dynamics argue for a merger origin in which the effects of gas were not very important (Matthias & Gerhard 1999). Terlevich & Forbes (2002) estimated the age of NGC 1600 to be 7.3 Gyr with $[\text{Fe}/\text{H}] = 0.41$, while Trager et al. (2000) estimated an age of ~ 8.8 Gyr with $[\text{Fe}/\text{H}] \sim 0.15$ through the inner 5.7" and ~ 4.6 Gyr and $[\text{Fe}/\text{H}] \sim 0.24$ through the inner 22.7". The colors (Sandage 1973; Frogel et al. 1978) of NGC 1600 are consistent with colors from NGC 3379, a prototypical elliptical galaxy, suggesting star-formation has not occurred recently. In addition to X-ray emitting gas, NGC 1600 also has cooler gas as indicated by $\text{H}\alpha$ (Trinchieri & di Serego Alighieri 1991) and dust (Ferrari et al. 1999). Post-AGB stars seem capable of producing the necessary ionization/heating for the $\text{H}\alpha$ and dust.

In § 2, we discuss the observations and data reduction of NGC 1600. After presenting the X-ray images in § 3, we discuss the properties of resolved sources in § 4. The spatial distribution of the diffuse X-ray emission and structures found in it are described in § 5, where they are compared to structures in other wavebands. We discuss the X-ray spectral properties of the sources and unresolved emission in § 6. We estimate the gas and gravitational mass in § 7. Finally, we summarize our conclusions in § 8.

2. OBSERVATION AND DATA REDUCTION

NGC 1600 was observed in two intervals (observations 4283 and 4371) on 2002 September 18–19 and September 20 with live exposures of 26,783 and 26,752 s, respectively. The ACIS-35678 chips were operated at a temperature of -120 C with a frame time of 3.2 s. We determined the pointings so that the entire galaxy was located on the S3 chip, with the galaxy center offset from the node boundaries of the chip. Although a number of serendipitous sources were seen on the other chips, the analysis in this paper is based on data from the S3 chip alone. The data were telemetered and cleaned in Very-Faint mode, and only events with ASCA grades of 0, 2, 3, 4, and 6 were included. Photon energies were determined using the gain file acisD2000-08-12gainN0003.fits and corrected for time dependence of the gain¹. We excluded bad pixels, bad columns, and columns adjacent to bad columns or chip node boundaries.

Chandra is known to encounter periods of high background (“background flares”), which especially affect the

backside-illuminated S1 and S3 chips². We determined the background count rate from the S1 chip to avoid the enhanced flux due to the galaxy on the S3 chip. Using Maxim Markevitch’s LC_CLEAN program², we found the exposure intervals that were unaffected by background flares. The first observation showed clear evidence of a major flare in the first 20% of the observation. The second observation had some small fluctuations greater than 20% from the mean rate. After these were filtered, observations 4283 and 4371 had flare-free exposure times of 21,562 and 23,616 s, respectively. We created a merged events file for imaging analysis after checking that the observations were well registered; the separate events files were used for spectroscopic analysis. We took the backgrounds for extended regions from the deep blank sky backgrounds compiled by Maxim Markevitch², adjusted them to the aspect histories of our observations, and changed the normalizations slightly to match the hard count rate (pha=2500:3000) of the blank-sky background with a relatively emission-free region on the S3 chip. For imaging analysis, we also included the “background” due to the readout artifact in ACIS using a script based on the MAKE_READOUT_BG program².

We performed the data reduction and some of the data analysis using the *Chandra* analysis package CIAO 2.3³ and NASA’s FTOOLS⁴. Spectra were fit using XSPEC⁵, while correcting for the ACIS quantum efficiency (QE) degradation⁶ with the XSPEC ACISABS model.

3. X-RAY IMAGE

NGC 1600 has a combination of diffuse emission and resolved point sources. In order to image the diffuse emission without deemphasizing the point sources, we adaptively smoothed the background-subtracted, exposure-corrected image using a minimum signal-to-noise ratio (S/N) per smoothing beam of 3. Figure 1 displays a true-color image of the adaptively smoothed X-ray image. This image was created by smoothing three exposure and background-corrected images in soft (0.3–1 keV), medium (1–2 keV), and hard (2–6 keV) bands using the same kernel required for the total band adaptively smoothed image, and then combining them with the color coding red = soft, green = medium, and blue = hard. A logarithmic intensity scale was chosen to range between total band surface brightnesses of $5 \times 10^{-7} \text{ counts arcsec}^{-2} \text{ s}^{-1}$ and $1 \times 10^{-3} \text{ counts arcsec}^{-2} \text{ s}^{-1}$.

In Figure 2, we show the corresponding Second Palomar Sky Survey (POSS II) optical (red) image using a linear gray scale. The field of view is the same as that in Figure 1. The largest galaxy near the upper center is NGC 1600, and corresponds to the brightest peak in the diffuse X-ray emission. Another group member, NGC 1603, lies to the east of NGC 1600. The galaxy north of NGC 1600 is the group member NGC 1601. On Figure 2, the overlaid regions indicate the positions of the X-ray sources discussed in § 4 and listed in Table 1. All of the sources with fluxes determined to $> 3\sigma$ (shown as

² See <http://cxc.harvard.edu/contrib/maxim/acisbg/>.

³ See <http://asc.harvard.edu/ciao2.3/>.

⁴ See <http://heasarc.gsfc.nasa.gov/ftools/>.

⁵ See <http://heasarc.gsfc.nasa.gov/docs/software/lheasoft/>.

⁶ See http://cxc.harvard.edu/cal/ACIS/Cal_prods/qeDeg/.

¹ See [http://hea-www.harvard.edu/\\$simalexey/acis/tgain/](http://hea-www.harvard.edu/$simalexey/acis/tgain/).

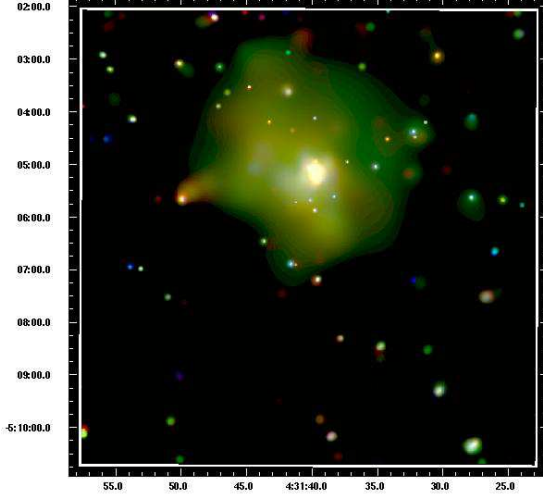


FIG. 1.— Adaptively smoothed *Chandra* true-color S3 image (with red = 0.3–1 keV, green = 1–2 keV, and blue = 2–6 keV) of NGC 1600, corrected for exposure and background. The total intensity scale is logarithmic and ranges from 5×10^{-7} counts $\text{arcsec}^{-2} \text{ s}^{-1}$ to 1×10^{-3} counts $\text{arcsec}^{-2} \text{ s}^{-1}$. The white square is the field of view of the *Chandra* S3 image.

squares) are clearly seen in the adaptively smoothed X-ray image (Figure 1), except for the central three sources that are embedded in strong diffuse emission. Very few of the weaker sources can be seen in Figure 1.

The diffuse X-ray emission in Figure 1 shows several interesting structures. The central X-ray emission of NGC 1600 is elongated in a direction which is roughly aligned with the optical emission. However, there are some structures in the central X-ray emission, which are discussed below (§ 5.1). The emission around the elliptical galaxy NGC 1603 in the east appears somewhat extended, and there is a bridge of X-ray emission extending from NGC 1603 to the west toward NGC 1600. There is an X-ray source associated with the lenticular galaxy NGC 1601, but it is unclear whether it is extended in this image. On larger scales, there is a slightly elongated region of very extended X-ray surface brightness, with excess diffuse emission to the northeast of NGC 1600. (Adaptively smoothed images with the sources replaced by Poisson noise do not affect the gross morphology of the diffuse X-ray emission; that is, these diffuse features are not due to the smearing of point sources.)

4. RESOLVED SOURCES

4.1. *Detections*

We used the wavelet detection algorithm (CIAO WAVDETECT program) with $\sqrt{2}$ scales ranging from 1 to 32 pixels to identify the discrete X-ray source population on the ACIS S3. Since the wavelet source detection threshold was set at 10^{-6} , $\lesssim 1$ false source (due to a statistical fluctuation in the background) is expected in the entire S3 image. Source detection was first performed on the separate observations to check their astrometric registration; no significant offset was found. To maximize S/N, we analyzed the wavelet detection results from the combination of the two observations. We required our sources have wavdetect fluxes determined at the $\geq 3\sigma$ level for all analyses except the identification of possible

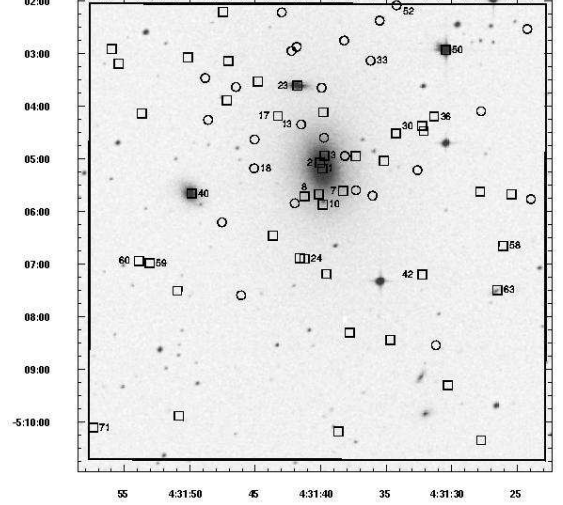


FIG. 2.— Linear gray scale POSS-II Red optical image of NGC 1600. The squares and circles indicate the positions of the X-ray sources with $S/N > 3$ and $S/N < 3$ in Table 1, respectively. Sources mentioned in the text are labeled. The dark square is the field of view of the *Chandra* S3 image.

optical counterparts.

At that level, the minimum detected count rate in the 0.3–6 keV band was 2.7×10^{-4} counts s^{-1} ; however, the bright diffuse gaseous emission at the center of the galaxy makes it difficult to establish a minimum detectable flux over the entire image. For backgrounds of < 0.05 counts pix^{-1} and off-axis distances appropriate to the S3 chip, sources with 20 counts should be detected at a roughly uniform completeness level ($\gtrsim 85\%$) (Kim & Fabbiano 2003). For sources satisfying these criteria, the minimum detected flux was 4.7×10^{-4} counts s^{-1} . To determine source characteristics other than their flux, we used a local background with an area three times that of each source's wavdetect region. In a few cases of nearby sources, the source or background regions initially overlapped. We slightly altered these overlapping regions, preserving the ratio of areas and the net count rates.

We also attempted detections in multiple bands (0.3–1, 1–2, 2–6 keV) and compared detection rates to the total band (0.3–6 keV). In these sub-bands, 45, 68, and 34% of the total band sources were detected, respectively. There were two, one, and five sources detected in an individual sub-band that were not detected in the total band. None of these extra detections had fluxes which were significant at the $\geq 3\sigma$ level. Two, eight, and five sources were detected in only one sub-band in addition to the total band, with two, six, and one of those sources having total band fluxes determined at $\geq 3\sigma$. In this X-ray bright galaxy, performing detections by sub-bands provided no advantage.

In Table 1, we list all discrete sources detected by WAVDETECT over the 0.3–6 keV range. The sources are ordered by increasing projected radial distance d from the center of the galaxy. Columns 1–8 provide the source number, the IAU name, the source position (J2000), the projected radial distance and semi-major distance a from the center NGC 1600, the wavdetect count rate with its 1σ error, and the S/N for the count rate. The fluxes

were corrected for exposure and the instrument PSF. The first three sources are clearly extended; when the count rate was determined using 1''.5 circular regions centered on the source centroid, none of those sources are significant at the 3σ level. Although the position of Source 1 is close to the optical/IR nucleus of NGC 1600, we are not confident it is a point source. Therefore, we adopted the 2MASS Point Source Catalog position of R.A. = $4^{\text{h}}31^{\text{m}}39\overset{\text{s}}{.}87$ and Dec. = $-5^{\circ}5'10\overset{\text{s}}{.}5$ as the location of the center of NGC 1600. All listed positions include astrometry corrections based on optical/IR counterparts (§ 4.2); the overall absolute astrometric errors are probably $\sim 0''.5$ near the field center, with larger errors further out.

In addition to the $\lesssim 1$ false source in the entire S3 field of view, some of the detected sources may be foreground or (more likely) background objects unrelated to NGC 1600. If we consider the fluxes of all our detected sources, we expect ≈ 48 unrelated sources based on the source counts in Brandt et al. (2000) and Mushotzky et al. (2000). Using the minimum detected $\geq 3\sigma$ flux, we expect ≈ 15 unrelated sources. Incompleteness will reduce both of these estimates, especially the first number. Unrelated sources should be spread out fairly uniformly over the S3 image (Figure 1), except for the reduced sensitivity at the center due to bright diffuse emission and at the outer edges of the field due to reduced exposure and increased PSF. Sources close to NGC 1600 are more likely to be associated with the galaxy, while sources far from NGC 1600 are more likely unrelated to NGC 1600.

4.2. Identifications

Sources in Table 1 were cross-correlated against optical/IR catalogs to identify possible counterparts and to improve the absolute astrometry of the observations. We used the Tycho-2 Catalog (Høg et al. 2000), 2MASS⁷ Point Source and Extended Source Catalogs⁸, and the USNO-B Catalog (Monet et al. 2003) to identify seven optical/IR counterparts to the X-ray sources. Four of these sources were used to determine the astrometry: Source 18 corresponds to USNO-B1 0849-0044132, an $R = 19.4$ mag object with a non-stellar PSF; Source 23 corresponds to NGC 1601, a nearby lenticular galaxy north of NGC 1600; Source 33 corresponds to 2MASS 04313613-0503081, a $J = 16.8$ mag star; and Source 50 corresponds to Tycho-2 4742-254-1, a $B = 11.7$ mag star. After correcting for an astrometric shift of about $0''.5$, the residual astrometric errors are $\approx 0''.5$.

We did not use the remaining three sources for astrometry since they were associated with extended X-ray or optical emission. The central source (Source 1) is $\approx 0''.9$ from the optical center of the galaxy (after the astrometric correction discussed above). As the X-ray source is extended, we used a 1''.5 radius circular region centered on the X-ray source to measure or limit the flux of any central point source; this gave a count rate of $(7.6 \pm 2.9) \times 10^{-4}$ counts s^{-1} (1σ error bars). Since this source was neither particularly hard nor detected very

⁷ See <http://www.ipac.caltech.edu/2mass/releases/second/doc/expsup.html>

⁸ When a source appeared in both 2MASS catalogs, the Point Source Catalog positions were used.

significantly as a point source, we conservatively adopt its 3σ upper limit luminosity of 6.7×10^{39} erg s^{-1} as an upper limit to a central active galactic nucleus (AGN).

Source 40 is $\approx 1''.7$ from the 2MASS center of NGC 1603, a nearby elliptical galaxy east of NGC 1600. There is clearly extended X-ray emission centered east of the source position that appears more coincident with the galaxy center. Since NGC 1603 extended well beyond this X-ray source (20 mag arcsec^{-2} isophotal K fiducial elliptical aperture semi-major axis, r_{K20fe} , of $18''.4$), Source 40 may be a point source offset from the center of NGC 1603. Similarly, Source 63 is $\approx 2''.9$ from 2MASX 04312667-0507309, a galaxy candidate whose r_{K20fe} is $7''.2$; Source 63 may also be a point source offset from this galaxy's center. Although Source 10 is close to an optical point source in Figure 2, the X-ray source is $\approx 3''.4$ south of the optical object; thus, we do not consider this to be a reliable optical identification for the X-ray source.

4.3. X-ray Luminosities and Luminosity Functions

To convert the source count rates into unabsorbed X-ray luminosities, we used the adopted *Chandra* X-ray spectrum (§ 6.1; Table 2, row 3) of the resolved sources to convert 0.3–6 keV count rates into 0.3–10 keV flux. We then assumed each source was at the distance of NGC 1600, 59.98 Mpc, yielding a conversion factor of 4.12×10^{42} erg count $^{-1}$. Column 8 of Table 1 lists the X-ray luminosities in units of 10^{38} erg s^{-1} , which range roughly from 2.8×10^{38} to 4.8×10^{40} erg s^{-1} . Since Sources 33 and 50 are likely foreground stars, their luminosities are probably overestimates.

By restricting the sample to the sources with a uniform completeness of 85% (≥ 20 net counts implying a count rate limit $\geq 4.7 \times 10^{-4}$ counts s^{-1} , and $d > 40''$ corresponding to a background $\lesssim 0.05$ counts pix^{-1} , § 4.1), excluding the sources corresponding to NGC 1601 (Source 23) and NGC 1603 (Source 40), and excluding the very bright source corresponding to a foreground Tycho star (Source 50), we created our analysis sample of 20 sources (see Notes in Table 1). We expect 11 ± 2 foreground/background sources based on the source counts in Brandt et al. (2000) and Mushotzky et al. (2000).

In Figure 3, we display the cumulative luminosity function (LF) of our analysis sample. The LF should be the sum of the point source (LMXB) population of NGC 1600 and the foreground/background population. We fit the LF using the same techniques we have used previously (Sarazin et al. 2000, 2001; Irwin, Sarazin, & Bregman 2002); a single power-law, broken power-law, and a cutoff power-law were all used to model the LMXB population. The background source population was modeled as discussed in the previous references. A single power-law fits the data very well based on the Kolmogoroff-Smirnov (KS) test:

$$\frac{dN}{dL_{39}} = N_0 L_{39}^{-\alpha}, \quad (1)$$

where $L_{39} \equiv L_X / (10^{39} \text{ erg s}^{-1})$. The best fit was determined by the maximum likelihood method, and the errors (90% confidence interval) were determined by Monte Carlo techniques. We found $N_0 = 21.1_{-10.0}^{+73.0}$ and $\alpha = 2.00_{-0.35}^{+1.14}$. Although a cutoff power-law is not required by the fits, the total luminosity of all of the sources

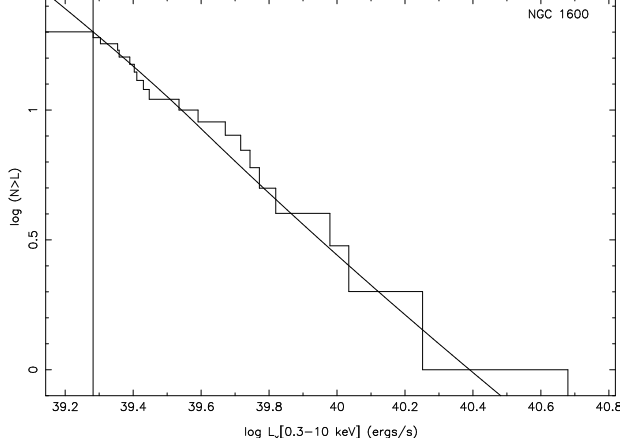


FIG. 3.— Histogram of the observed cumulative luminosity function of resolved sources in our analysis sample. The continuous curve is the sum of the best-fit LMXB luminosity functions (eq. 1) and the expected background source counts. The vertical line indicates the completeness limit of our sample.

diverges at the high luminosity limit for the best-fit LF. The lack of very bright sources (beyond those observed) in NGC 1600 can be explained by Poisson fluctuations; however, it seems likely that the correct underlying LF of the sources in NGC 1600 is either a bit steeper than the best-fit value, or that it steepens or has a cut-off at high luminosities beyond those observed.

Early-type galaxies tend to have broken or cut-off power-law LFs with the break or cutoff occurring well below the luminosities measured in NGC 1600, while star forming galaxies tend to have single power-law LFs that extend to low luminosities (Sarazin et al. 2001; Blanton et al. 2001; Finoguenov & Jones 2002; Zelas & Fabbiano 2002; Jeltema et al. 2003; Sivakoff, Sarazin, & Irwin 2003; Randall, Sarazin, & Irwin 2004). The high luminosities of the sources in NGC 1600 make it difficult to directly compare its luminosity function to other galaxies. Therefore, one must either extrapolate the NGC 1600 LF down to lower luminosities or extrapolate the LF of other galaxies to higher luminosities in order to compare them. The differential LF slopes at the highest luminosities in early-type galaxies tend to be steeper than 2.5, and tend to cluster around 1.5 in galaxies with some level of star formation. The best-fit slope of NGC 1600 is intermediate between the two; however, within the errors, the slope is more consistent with the other early-type galaxies. The normalization of NGC 1600 is higher by at least a factor of four than in any of the galaxies in the above references. Extrapolating the best-fit luminosity function, we would find ~ 40 and ~ 420 sources above 5×10^{38} erg s $^{-1}$ and 5×10^{37} erg s $^{-1}$, typical break luminosities and minimum observed luminosities in other early-type galaxy observations. If there is a break in the luminosity function below 2×10^{39} erg s $^{-1}$, the numbers of fainter sources would be reduced.

Only one of the sources in the analysis sample is fainter than 2×10^{39} erg s $^{-1}$. There are six additional sources which could qualify as ULX candidates, Sources 1–3, 7, 52, and 71. Since Sources 1–3 appear extended, we used a

1. $5''$ radius circular region to measure the flux of a possible point source. The count rates of Sources 1 and 2 are sufficient to qualify as ULX candidates; however, their fluxes are not determined at the 3σ limit. Of the remaining candidates, only Sources 7 and 71 are ULX candidates with well-determined fluxes. Source 7 is not included in the analysis sample since it is only $35''$ from the nucleus of NGC 1600. Source 71, a source at the edge of the chip did not make it into the analysis sample due to its small number of counts, ~ 17 ; its luminosity is boosted by a large exposure correction. Including Sources 7 and 71, we observe 21 ULX candidates. At the flux limit corresponding to $L_X = 2 \times 10^{39}$ erg s $^{-1}$, we expect 11 ± 2 foreground/background sources based on the source counts in Brandt et al. (2000) and Mushotzky et al. (2000) for the entire chip. The number of ULX candidates in excess to the expected background is 10 ± 5 . Even if we consider sources with $L_X > 4 \times 10^{39}$ erg s $^{-1}$, there are ten ULX candidates and only ≈ 5 unrelated foreground/background sources are expected. This corresponds to an excess of 5 ± 3.3^9 . The error budgets of both excesses are dominated by Poisson counting errors in NGC 1600.

In a sample of 28 early-type galaxies, the number of sources with $L_X \geq 2 \times 10^{39}$ erg s $^{-1}$ (0.3–10 keV) was equivalent to the expected number of foreground/background sources (Irwin et al. 2004)¹⁰. Although the number of ULX candidates is greater than the average number of unrelated sources, the number of ULX candidates in NGC 1600 could be a result of cosmic variance in the foreground/background sources. One item in support of this possibility is that the fitted slope of the luminosity function is consistent with the typical slopes of foreground/background luminosity functions (Brandt et al. 2001; Giacconi et al. 2001). To examine the possibility of cosmic variance, we compared the source densities we observed to the 0.5–2.0 keV source densities of the Chandra Deep Fields¹¹.

Within two D25 ($a \leq 147''$), the observed source density of ULX candidates in NGC 1600 is 2250 ± 796 deg $^{-2}$, while the remaining field of the S3 chip has a source density of 884 ± 245 deg $^{-2}$. In order to compare the background source densities with those in Brandt et al. (2001) and Giacconi et al. (2001), we converted our count rates to energy fluxes in the 0.5–2.0 keV band using a $\Gamma = 1.4$ power-law spectrum. Then, the minimum detectable 0.5–2.0 keV flux for our observation of NGC 1600 is 1.36×10^{-15} erg cm $^{-2}$ s $^{-1}$. The Chandra Deep Fields predict foreground/background source densities of $\sim 690 \pm 260$ deg $^{-2}$ (North) and 520 ± 110 deg $^{-2}$ (South). Assuming a background source density of 600 ± 100 deg $^{-2}$, there is an $\sim 2.1\sigma$ excess within two D25 of the galaxy corresponding to an excess of $\sim 6 \pm 3$ sources. The errors are dominated by counting errors in NGC 1600 as opposed to uncertainty in the background source density. The excess near the galaxy favors an as-

⁹ We use \sqrt{N} statistics since they better represent the true low-count Poisson lower limit 1σ confidence level than the Gehrels approximation of $1 + \sqrt{N + 0.75}$ (Compare with eq. [7], eq. [11], and Table 2 in Gehrels (1986)).

¹⁰ This study used surface brightness profile distances which are consistent with $H_0 = 74 \pm 4$ km s $^{-1}$ Mpc $^{-1}$ (Tonry et al. 2001).

¹¹ We chose to use the 0.5–2.0 keV band since all but one of the ULX candidates were detected in soft as well as hard bands.

sociation of ULX candidates with NGC 1600; however, cosmic variance cannot be ruled out.

When one subdivides the ULX candidates into a fainter sample $L_X = 2-4 \times 10^{39}$ erg s $^{-1}$ and a brighter sample, $L_X > 4 \times 10^{39}$ erg s $^{-1}$, we find that the brighter sample source densities are more consistent with the background than the fainter sample. In particular, there are no sources in the bright sample, which has better completeness than the faint sample, within two effective radii; in the faint sample, there are four sources. One possible explanation is that the overabundance of the bright ULX candidates is due to cosmic variance of foreground/background sources, while the overabundance of the faint ULX candidates is from sources within NGC 1600. The ULX candidates could then be brought more in line with the findings of Irwin et al. (2004) by a coincidence of cosmic variance and a $\sim 40\%$ overestimate in the distance to NGC 1600. Such large differences do occasionally occur between recessional velocity distances and surface brightness fluctuation distances; however, in the case of NGC 1600, this would require NGC 1600 have a peculiar velocity of $\sim +1300$ km s $^{-1}$. Since this peculiar velocity is more typical of cluster infall and there is no nearby large cluster, we do not think this model is likely.

If cosmic variance does not explain the excess number of bright sources, then these bright sources are actually ULX candidates associated with NGC 1600. NGC 1399 has three sources with $L_X \geq 2 \times 10^{39}$ erg s $^{-1}$, the largest number at these luminosities among previously observed early-type galaxies. NGC 1407 may have five such sources; however, its distance is highly uncertain (Irwin et al. 2003). Although Jeltema et al. (2003) find that NGC 720 has nine ULX candidates, only one has a luminosity $\geq 2 \times 10^{39}$ erg s $^{-1}$ for $H_0 = 75$ km s $^{-1}$ Mpc $^{-1}$. Thus, we believe that NGC 1600 may have the largest number of ULX candidates brighter than 2×10^{39} erg s $^{-1}$ observed in an early-type galaxy to date.

There are a variety of models explaining the presence of ULX sources. Some of these include favorable viewing angles of anisotropic radiation (King et al. 2001), super-Eddington accretion by high mass X-ray binaries (HMXBs) at the thermal-timescale mass transfer rate (King 2002), accretion onto intermediate-mass black holes (Colbert & Mushotzky 1999), super-Eddington accretion of LMXBs in the soft X-ray transient state (King 2002), and super-Eddington accretion from thin accretion disks of stellar mass black holes (Begelman 2002). If anisotropic radiation was the cause of ULXs in NGC 1600, one would predict the existence of a large population of ULXs seen at fainter fluxes, due to misalignment with the preferred axis of the anisotropic radiation, in addition to the intrinsically faint and isotropic radiating LMXB populations; our observation doesn't go deep enough to observe such sources.

Since NGC 1600 has an observed age of 7.3 Gyr (Terlevich & Forbes 2002) and its photometric colors (Sandage 1973; Frogel et al. 1978) are typical for an elliptical galaxy, one would not expect its X-ray binaries to be HMXBs. Comparisons of the FIR detections of NGC 1600 from IRAS in the 60μ and 100μ bands with the radio flux (Birkinshaw & Davies (1985)) could be consistent with either AGN or stellar heating of interstellar dust (Condon & Broderick 1991).

Trinchieri & di Serego Alighieri (1991) and Ferrari et al. (1999) both found that post-AGB stars are the likely source of the ionization of the gas and heating of the dust in NGC 1600. Thus, the FIR detections do not necessarily indicate that there is recent star formation as needed for HMXBs. Additionally, the cumulative spectrum of the ULX candidates in NGC 1600 is not consistent with the disk blackbody model found to fit well in ULXs associated with spiral galaxies (Makishima et al. 2000).

Intermediate-mass black holes may be created if the progenitor mass of a star is $\gtrsim 40 M_\odot$ (Fryer & Kalogera 2001) and that star sinks to the center of a globular cluster where it can grow up to $\sim 10^3 M_\odot$ in 10^{10} years (Miller & Hamilton 2002). Under this model, NGC 1600 would be expected to have a large number of globular clusters. The LMXB-GC connection in early-type galaxies (Sarazin et al. 2000, 2001; Angelini et al. 2001; Kundu et al. 2003; Sarazin et al. 2003) means that LMXBs in the soft X-ray transient state or black hole LMXBs with thin accretion disks would also be consistent with a large number of globular clusters. Thus, it seems plausible that the large population of ULXs in NGC 1600, if they are not due to cosmic variance in the number of unrelated sources, requires a large population of GCs. Unfortunately, the globular cluster population of NGC 1600 does not appear to have been determined.

4.4. Hardness Ratios

Hardness ratios or X-ray colors are useful for crudely characterizing the spectral properties of sources, and can be applied to sources that are too faint for detailed spectral analysis. We determined the observed X-ray hardness ratios for the sources, using the same techniques we used previously (Sarazin et al. 2000, 2001; Blanton et al. 2001; Irwin et al. 2002). We define three hardness ratios as $H21 \equiv (M-S)/(M+S)$, $H31 \equiv (H-S)/(H+S)$, and $H32 \equiv (H-M)/(H+M)$, where S , M , and H are the total counts in the soft (0.3–1 keV), medium (1–2 keV), and hard (2–6 keV) bands, respectively. As compared to our previous definitions, we have reduced the hard band from 2–10 keV to 2–6 keV. Since the 6–10 keV range is dominated by background photons for most sources, this should increase the S/N of the hardness ratio techniques. The hardness ratios measure observed counts, which are affected by Galactic absorption and QE degradation in the *Chandra* ACIS detectors. In order to compare to other galaxies, it is useful to correct the hardness ratios for these two soft X-ray absorption effects. Therefore, we have calculated the intrinsic hardness ratios, denoted by a superscript 0, using a correction factor in each band appropriate to the best-fit spectrum of the resolved sources. The intrinsic hardness ratios and their 1σ errors are listed in columns 10–12 of Table 1.

Although we have plotted $H31$ vs. $H21$ in the past, plots of $H32$ vs. $H21$ allow for better separation of simple spectral models. In Figure 4 we plot both $H31^0$ vs. $H21^0$ and $H32^0$ vs. $H21^0$ for the 20 sources in the analysis sample. The hardness ratios for the sum of those sources are $(H21^0, H32^0, H31^0) = (-0.26, -0.39, -0.59)$; the uncorrected hardness ratios are $(H21, H32, H31) = (+0.11, -0.33, -0.24)$. Sources with ~ 40 net counts had errors similar to the median of the uncertainties, ~ 0.2 . The errors scale roughly with the inverse square root of the net counts.

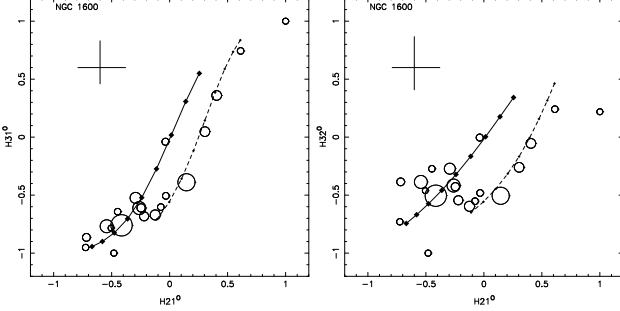


FIG. 4.— Hardness ratios for the sources in our analysis sample. Here, $H21^0 \equiv (M^0 - S^0)/(M^0 + S^0)$, $H31^0 \equiv (H^0 - S^0)/(H^0 + S^0)$, and $H32^0 \equiv (H^0 - M^0)/(H^0 + M^0)$, where S^0 , M^0 , and H^0 are the counts in the soft (0.3–1 keV), medium (1–2 keV), and hard (2–6 keV) bands, corrected for the effect of Galactic absorption and QE degradation according to the best-fit spectra of resolved sources. The area of each circle is proportional to the observed number of net counts. The solid curve and large diamonds show the hardness ratios for power-law spectral models; the dashed curve and small diamonds show the ratios for intrinsic absorption of $N_H = 4 \times 10^{21} \text{ cm}^{-2}$; the diamonds indicate values of the power-law photon number index of $\Gamma = 0$ (upper right) to 3.2 (lower left) in increments of 0.4. Both models underwent the same correction as the sources. The 1σ error bars at the upper left illustrate the median of the uncertainties.

In previously studied galaxies, most of the sources lie along a broad diagonal swath extending roughly from $(H21, H31) \sim (-0.3, -0.7)$ to $(0.4, 0.5)$. Usually, these hardness ratios were not corrected for Galactic absorption and QE degradation; the latter effect was not known at the time of some of the previous studies. Since there are fewer sources and the absorption/degradation corrections tend to push sources to the lower-left part of the diagram, this swath is less evident in NGC 1600. In Figure 4, the solid line corresponds to hardness ratios for power-law source spectra with $\Gamma = 0$ –3.2. In calculating these model hardness ratios, Galactic absorption and QE degradation were applied to the model spectra, and the hardness ratios were corrected for these effects using the best-fit spectral model of the resolved sources as described above. The dashed line corresponds to a similar model, with an intrinsic absorbing column of $4 \times 10^{21} \text{ cm}^{-2}$. Most of the sources are consistent with $\Gamma = 1.6$ –2.2, with the sum of these sources corresponding to $\Gamma \approx 1.7$. The majority of the sources lie roughly between the two models in $H31^0$ vs. $H21^0$. In $H32^0$ vs. $H21^0$, we see that most of the sources have an $H32^0 \sim -0.5$, but the two models still roughly contain the sources. When compared to the $H31^0$ vs. $H21^0$ plot, the effects of absorption in the $H32^0$ vs. $H21^0$ plot are larger, and the effects of absorption and varying power-law index are more nearly orthogonal. Although it is suggestive that the sources tend to lie on one of the two tracks, the errors are large and the number of the sources is small, so this could be a coincidence.

In NGC 4697 and the bulge of NGC 1291, a total of four sources had $(H21, H31) \approx (-1, -1)$. Scaling from the number of sources in NGC 4697, one would have only expected ~ 2 supersoft sources in NGC 1600, so the lack of any strong candidates is not surprising. Moreover, the supersoft sources in NGC 4697 would all have been below our detection limit at the distance of NGC 1600. Another problem is that the soft X-ray response of the *Chandra*

ACIS S3 detector was much worse at the time NGC 1600 was observed due to QE degradation⁶. Although the hardness ratios are corrected for this effect, the correction is based on the average (hard) spectrum of the sources; this correction would be too small for supersoft sources. Supersoft sources in NGC 1600 would have been hard to detect unless they were very bright.

Among the sources with $> 3\sigma$ known fluxes, we find three sources (42, 58, and 60) with very hard spectra, $(H21^0, H31^0) > (0.5, 0.5)$, and three sources (17, 36, and 50) with little hard emission, $H31^0 \sim -1.0$. The very hard sources may be unrelated, strongly absorbed AGNs, similar to the sources which produce the hard component of the X-ray background, and which appear strongly at the faint fluxes in the deep *Chandra* observations of blank fields (Brandt et al. 2000; Mushotzky et al. 2000; Giacconi et al. 2001); however, all three sources have large hardness ratio errors. The sources without hard emission may also be unrelated foreground/background sources as indicated by studies of other galaxies (Sarazin et al. 2001) and deep blank sky images (e.g., Giacconi et al. 2001); Source 50 (See § 4.2) is clearly a foreground object, while Source 36 has large hardness ratio errors.

The hardness ratios of Sources 1–3 are softer than a majority of the sources in the analysis sample; however the errors of Sources 2 and 3 could bring them more in line with the analysis sample. Since these extended sources appear softer, it is more likely that they are small scale structures in the diffuse gas (See § 5.2), than that they are a number of confused sources.

4.5. Variability

With two observations we could test for variability on two time scales, intra-observation, and inter-observation. Since the mid-points of the observations were only ~ 60 ks apart, the timescales are not remarkably different. We searched for variability in the X-ray emission of the resolved sources over the duration of the *Chandra* observations individually and jointly using the KS test (see Sarazin et al. 2001). Additionally, we compared the count rates between the two observations. In Table 1, we report the sources that had a $> 95\%$ variability probability in any one of these four tests. Among the 43 3σ flux detected sources away from the edge of the chip, Sources 1, 8, 24, 30, and 59 were apparently variable. Source 1 had a 2.1σ (96% probability) rate decline in count rate between the two observations; however, the variability was not significantly detected within the individual observations. This suggests that there may be a point source variable on a timescale > 20 ks buried in the diffuse emission of this extended source. The flux in a $1''5$ circular region centered on the position of Source 1, which includes the galaxy center, is nearly constant between the two observations. This suggests that the buried variable point source, if it exists, is not a central AGN. For Source 8, the KS test on the joint observations yielded a 95% probability of variability. Source 24 shows a variability at the 99% probability in the first observation; in this observation, six of its seven counts occur within ~ 4 ks. Source 30 undergoes a 2.0σ (95% probability) rate increase between the two observations. Finally, Source 59 has a 98% probability of being variable in the joint observation KS test. With 43 sources, ~ 2

false positives are expected at a $> 95\%$ limit. Of the four sources variable at this limit, Sources 24 and 59 show the strongest behavior of variability, both in the form of outbursts. Although Source 71 shows 95% variability in the first observation, its lightcurve is irregularly sampled due to its location at the edge of the chip. Source 13, a weakly detected source, had a very high variability probability, 99%, in the second observation since all three counts in that observation occurred in the last 750 seconds. The remaining weak sources that are marked as potentially variable did not exhibit such clearly variable behavior as in Source 13.

5. UNRESOLVED X-RAY EMISSION

As mentioned in § 3, the morphology of the unresolved X-ray emission is complex. This emission is a combination of unresolved point sources and diffuse gaseous emission. Ideally, we would like to use the spectral properties of the gas and resolved sources (See § 6) to disentangle the two as in Sarazin et al. (2001) and Sivakoff et al. (2003); however, the changing diffuse gas temperature of NGC 1600 does not allow this separation. For this reason, we chose to use the entire 0.3–6 keV band in analyzing the unresolved emission of NGC 1600. From the spectral fits, we estimate unresolved point sources contribute $\sim 30\%$ of the total unresolved counts. For comparisons with previous studies, we left in resolved sources with $S/N < 3$. As Source 1 may be the peak of the unresolved emission, we did not exclude it. Since Sources 2 and 3 were extended, we only excluded regions corresponding to $1''.5$ circular regions located at their centers. We used the blank-sky background to statistically remove background events.

5.1. Radial Profile of the Unresolved X-ray Emission

In order to compare the spatial distribution of the unresolved X-ray emission in NGC 1600 with the optical emission by stars, we adopted the Third Reference Catalogue of Bright Galaxies (RC3) values for the optical photometry's effective radius ($r_{\text{eff}} = 45''.4$), position angle ($PA = 15$), and ellipticity ($e = 0.324$), which assumes a de Vaucouleurs profile (de Vaucouleurs et al. 1992). The corresponding semi-major axis, a_{eff} is $55''.2$. Although Rembold et al. (2002) find a different profile in the infrared (a Sérsic profile with $n \sim 1\text{--}2$, an effective radius of $\sim 10\text{--}15''$, a semi-major axis position angle of $\sim 10\text{--}20$, and ellipticity of 0.17–0.34), the values of the position angle and ellipticity are roughly consistent with the optical profile. The corresponding semi-major axis is $17''.6$ using the optical ellipticity. Since the effective radius is only used for scaling in this paper, the large discrepancy between the two radii does not make a difference in our study.

We determined the surface brightness profile (SBP; Figure 5) and the hardness ratios (Figure 6) for a series of elliptical annuli with semi-major widths of $5''$, extending to $180''$. We could have used much narrower annuli near the center of NGC 1600, but there is significant non-axially-symmetric structure in the image there (§ 5.2 below). In the SBP, the dotted line displays the (optical) best-fit de Vaucouleurs profile with effective semi-major axis fixed at $55''.2$ and the dashed line displays the (J-band) best-fit Sérsic $n = 1.65$ profile with effective semi-major axis fixed at $17''.6$. The normalizations of the

optical profiles were varied to achieve the best fit. It is clear that neither the optical nor the infrared profile fit the unresolved X-ray emission well.

We first tried to fit the SBP using a single beta model profile,

$$I_X(a) = I_0 \left[1 + \left(\frac{a}{a_c} \right)^2 \right]^{-3\beta+1/2}, \quad (2)$$

where a_c is the core semi-major axis. However, that model was clearly rejected with a χ^2 of 431 for 33 degrees of freedom (dof). The best-fit single beta model has a small core radius a_c , leading to essentially a power-law model. The model underestimates the emission in the inner $20''$ and beyond $90''$ while overestimating the emission between $20''$ and $60''$. Figure 5 clearly shows that there are at least two components to the X-ray SBP of NGC 1600. Thus, we tried to fit the SBP with a double beta model:

$$I_X(a) = I_{0,\text{inner}} \left[1 + \left(\frac{a}{a_{c,\text{inner}}} \right)^2 \right]^{-3\beta_{\text{inner}}+1/2} + I_{0,\text{outer}} \left[1 + \left(\frac{a}{a_{c,\text{outer}}} \right)^2 \right]^{-3\beta_{\text{outer}}+1/2}. \quad (3)$$

The core radius of the outer component $a_{c,\text{outer}}$ is poorly determined and consistent with zero. That is, the outer part of the SBP could be fit by a power-law surface brightness; however, a pure power-law form would produce a peak in the X-ray SBP at the very center which is not seen in the image. Therefore, we chose to freeze the outer core semi-major axis at $25''$. We then found $I_{0,\text{inner}} = 0.97^{+0.08}_{-0.07}$ counts $\text{s}^{-1} \text{arcmin}^{-2}$, $a_{c,\text{inner}} = 14.4^{+3.3}_{-2.3}$ arcsec (4.2 kpc in projection), $\beta_{\text{inner}} = 1.18^{+0.33}_{-0.20}$, $I_{0,\text{outer}} = 0.039^{+0.005}_{-0.005}$ counts $\text{s}^{-1} \text{arcmin}^{-2}$, $a_{c,\text{outer}} \equiv 25.0$ arcsec (7.3 kpc in projection), and $\beta_{\text{outer}} = 0.36^{+0.01}_{-0.01}$. The values of this fit were consistent with the error bars from the double beta model profile with a free outer core semi-major axis, and the χ^2 of this fit, 39.0 for 30 dof, was only 0.9 higher. Therefore, we adopted this fit, the solid-line in Figure 6, as the best-fit SBP model. To ensure that the inclusion of Source 1 did not affect the fit, we attempted to fit the same model without using the first annulus. The new fit was within the error bars of the above fit.

A β of 1.18 is much larger than in most X-ray bright galaxies (Forman et al. 1985; Trinchieri et al. 1986). However, these previous fits were done with a single beta model and on much poorer resolution data. Below, we will argue that the inner beta model component of the SBP is interstellar gas in NGC 1600, while the outer beta model component is intragroup gas. It may be that the intragroup medium has compressed the galactic gas, decreasing the value of a_c and steepening the profile (increasing β).

Figure 6 shows the profiles of the hardness ratios for the unresolved emission. As was true for the SBP, the hardness ratio profiles show a break in behavior at $a \sim 25''$. The inner regions of the galaxy are noticeably softer than outer regions. It is unlikely that this trend is due to unresolved point stellar sources. The optical profile of the galaxy is more centrally condensed than the X-ray SBP (Figure 6), so unresolved stellar sources should

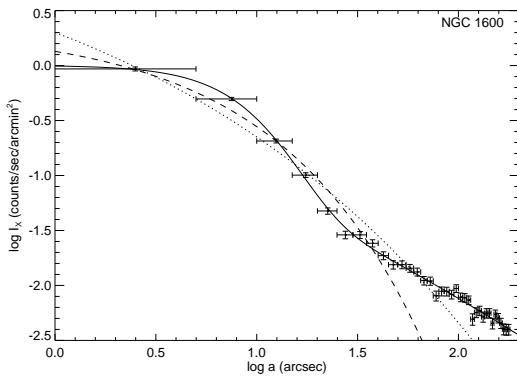


FIG. 5.— Surface brightness profiles, with 1σ error bars, of the unresolved emission (0.3–6 keV) as a function of projected semi-major axis a . The dotted and dashed curves show the RC3 de Vaucouleurs profile and J-band Sérsic profile, respectively, with fixed effective radii and normalizations varied to fit the X-ray surface brightness. The solid curve is the best-fit double beta model profile. All fits were for $a < 180''$.

contribute more in the inner regions. Yet, the average spectrum of the resolved sources is much harder than any of the diffuse emission, and would not cause the central regions of the diffuse emission to be softer. A positive temperature gradient and/or abundance gradient in the diffuse gas in the inner regions is the likely cause for the softer emission; in § 6.2 below, we show that the X-ray spectra do indicate that this change in the hardness is due to a temperature gradient.

5.2. Structural Features in the Unresolved X-ray Emission

In Figure 7, we display images where the resolved sources were replaced by the appropriate local Poisson noise. In each image, a cross marks the center of NGC 1600. On the left, we display the adaptively smoothed image of the total X-ray emission (0.3–6 keV) with logarithmic gray scale ranging from 1×10^{-6} counts $\text{arcsec}^{-2} \text{s}^{-1}$ to 2.9×10^{-4} counts $\text{arcsec}^{-2} \text{s}^{-1}$. From this image, we subtracted the double beta elliptical SBP; the excess emission image is shown in the middle panel with both limits of the gray scale reduced by a factor of two. The tail extending from NGC 1603 to the west toward NGC 1600 is shown clearly. This image shows that there is extended, diffuse emission around both of the smaller galaxies NGC 1601 and NGC 1603. There is some interesting residual structure near the center of NGC 1600, which is discussed in more detail below (§ 5.3). The structure near the center includes an excess emission region to the west of the center of NGC 1600. On larger scales, there is excess X-ray emission to the east and northeast of NGC 1600. In the right panel of Figure 7, we display the hardness ratio image (5'' Gaussian smoothed) of $H41 \equiv (H + M - S)/(H + M + S)$ between -0.4 (black) and 0.4 (white). This displays the softer central emission well. One can also see that the NGC 1603 tail appears softer than its surroundings. These features are also evident in Figure 1.

To quantify the surface brightness differences associated with the features in Figure 7, we determined the X-ray surface brightness of the unresolved emission in a number of elliptical annular pie regions. For each annu-

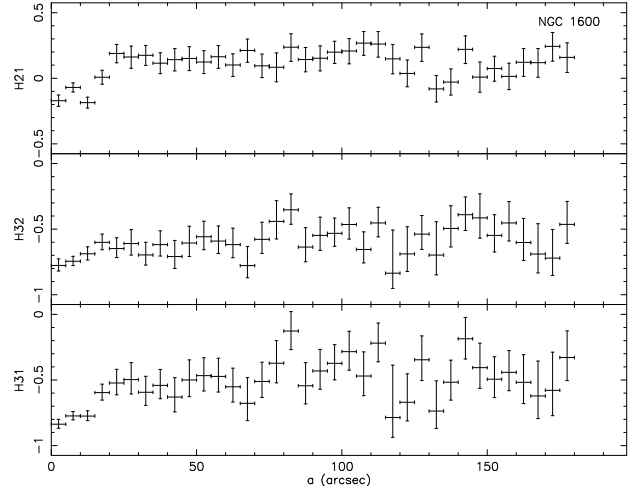


FIG. 6.— Hardness ratios with 1σ error bars for the unresolved emission as a function of semi-major axis a . Here, $H21 \equiv (M - S)/(M + S)$, $H31 \equiv (H - S)/(H + S)$, and $H32 \equiv (H - M)/(H + M)$, where S , M , and H are the observed counts in the soft (0.3–1 keV), medium (1–2 keV), and hard (2–6 keV) bands.

lus, we subdivided the region by PA (Figure 8). To quantify non-uniform morphology, we first fit a constant line to the surface brightnesses at each annulus (the dashed-line), iteratively excluding PA regions from the fit that diverged by more than 2σ . In the innermost annulus, emission from unresolved point sources and any inaccuracies from using the optical isophotes will be largest. Additionally, there appear to be small depressions in the emission just to the north and the south of the galaxy center, and a larger depression at the east edge of the annulus. These make it difficult to accurately establish a baseline for this annulus. There is a clear excess of emission ($PA = 255^\circ - 345^\circ, \gtrsim 4.3\sigma$) to the west of the second annulus. This excess continues in the third annulus ($PA = 255^\circ - 315^\circ, \gtrsim 3.0\sigma$), where an excess also appears 180 deg away ($PA = 105^\circ - 135^\circ, \sigma \gtrsim 5.6$). In the fourth and fifth annulus, the western excess has disappeared, while the eastern excess begins to take up most of the northeast quadrant ($PA = 30^\circ - 120^\circ, \gtrsim 4.0\sigma$). In the fourth annulus, there is also an isolated excess in the south ($\sim 3.5\sigma$). Finally, the last annulus clearly shows the NGC 1603 tail ($\sim 4.5\sigma$).

The excess to the northeast of NGC 1600 in annuli 3–5 of Figure 8 may be due to gas associated with the NGC 1600 group potential rather than the galaxy. We note that this northeast excess starts at about the same radius where the X-ray surface brightness profile in Figure 5 has an inflection point and the larger scale component dominates. This suggests the gas at these radii is responding to a potential with a larger scale. Both of these suggest that the outer gas is bound to the group, and that the center of the group potential is to the northeast of NGC 1600.

We believe that the tail west of NGC 1603 is the result of ram pressure stripping. NGC 1603 is at a projected distance from NGC 1600 of ~ 44.5 kpc with its velocity redshifted from NGC 1600 by ~ 284 km s^{-1} . Since NGC 1603 is part of the NGC 1600 group, we assumed that they were at the same distance. Given the tail seen in the X-ray image, it is unlikely that the

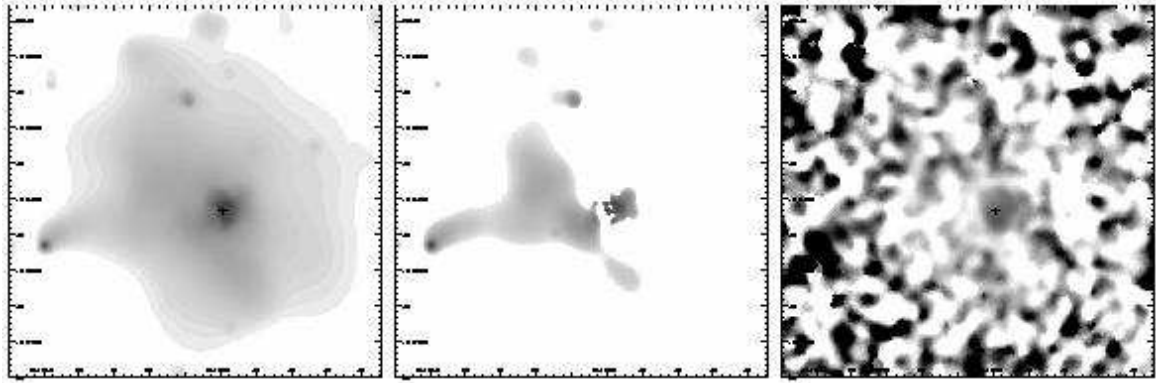


FIG. 7.— (Left) Adaptively smoothed *Chandra* S3 image (0.3–6 keV) of NGC 1600, with sources removed and corrected for exposure and background. The gray scale is logarithmic and ranges from 1×10^{-6} counts $\text{arcsec}^{-2} \text{ s}^{-1}$ to 2.9×10^{-4} counts $\text{arcsec}^{-2} \text{ s}^{-1}$. (Middle) The image on the left minus the best-fit double beta model surface brightness profile. The gray scale is also logarithmic and ranges from 5×10^{-7} counts $\text{arcsec}^{-2} \text{ s}^{-1}$ to 1.4×10^{-4} counts $\text{arcsec}^{-2} \text{ s}^{-1}$. (Right) The image of the hardness ratio $H41 \equiv (H + M - S) / (H + M + S)$, Gaussian smoothed with $\sigma = 5''$. The gray scale is linear and ranges from -0.4 (black) to 0.4 (white). In each image, a cross marks the center of NGC 1600.

only component of the velocity of NGC 1603 relative to NGC 1600 is along the line of sight. We assume that the two transverse components of the relative velocity are each about the same as the line of sight component. Thus, the total relative velocity of NGC 1603 is about $\approx \sqrt{3} \times 284 \text{ km s}^{-1} \approx 490 \text{ km s}^{-1}$. This would be a reasonable value for a circular orbital velocity for NGC 1603 around NGC 1600, whose observed radial velocity dispersion is 321 km s^{-1} (Faber et al. 1989). We argued above that there may be a significant potential associated with the NGC 1600 group, which would increase the estimated velocity.

We estimated the gas densities and pressures in NGC 1603 and in its environment to see if ram pressure could be sufficient to strip gas and form the tail. For the gas in NGC 1603, we assumed three uniform density spherical annuli with widths of $2''$ each. Since the X-ray emission from NGC 1603 is softer than the center of NGC 1600, we assume a spectrum with $kT = 0.6 \text{ keV}$ and solar abundances for the gas in this galaxy. With these assumptions, we find that the electron number densities of the gas in NGC 1603 are 4.9×10^{-2} , 1.9×10^{-2} , and $5.4 \times 10^{-3} \text{ cm}^{-3}$ and the pressures, P_{gas} , are 9.4×10^{-11} , 3.6×10^{-11} , and $1.0 \times 10^{-11} \text{ dyne cm}^{-2}$ in the $0\text{--}2$, $2\text{--}4$, and $4\text{--}6''$ annuli. We estimated the density in the group gas around NGC 1603 from the X-ray surface brightness in a hemispherical annulus centered on NGC 1603 (radius from NGC 1600 = $6''\text{--}12''$, $PA = 0^\circ\text{--}180^\circ$). This surface brightness agrees within the errors with the prediction by the modeled surface brightness profile at the semi-major distance of NGC 1603 from NGC 1600. We assumed a spectrum with $kT = 1.5 \text{ keV}$ and solar abundances. This gave an ambient gas electron density of $4.0 \times 10^{-3} \text{ cm}^{-3}$ at the projected semi-major distance of NGC 1603. Assuming a relative velocity of 490 km s^{-1} , the ram pressure of the ambient gas would be $P_{\text{ram}} \approx 1.6 \times 10^{-11} \text{ dyne cm}^{-2}$. The ram pressure would be lower if NGC 1603 is at a larger radius than its projected radius (i.e., in front of or behind the center of the NGC 1600 group). Roughly speaking, the condition for ram pressure to strip the gas is that $P_{\text{ram}} > P_{\text{gas}}$, which appears plausible in the outer $4\text{--}6''$ of NGC 1603. Since the tail points to

the west towards the higher density gas near NGC 1600, the ambient gas density may have been higher in the past, making ram-pressure stripping easier than it is at its present position.

The NGC 1603 tail has a softer spectrum (Figure 7 right) than the surrounding gas. Hardness ratios from counts in the same pie annuli used to construct Figure 8 confirm that the tail is softer in H21 by $\approx 2.6\sigma$. Thus, the jump in emission due to the tail is dominated by a jump in soft emission, consistent with ram-pressure stripping of cooler galactic gas by hotter group gas.

NGC 1601 also has a velocity redshifted from NGC 1600 by $\sim 309 \text{ km s}^{-1}$, and its projected distance from NGC 1600 is only $\sim 28.5 \text{ kpc}$. Since the emission associated with NGC 1601 is fainter, its estimated thermal pressure is smaller than in NGC 1603. This, combined with its slightly higher velocity, suggests that ram-pressure stripping should be stronger in NGC 1601 compared to NGC 1603. Although there is a hint of a tail toward the east of NGC 1601 in Figure 7, it has only a 1.3σ significance when the surface brightness in a hemispherical annulus east of NGC 1601 is compared to a similar annulus west of NGC 1601. There are a number of possible explanations of why we do not see a significant tail around NGC 1601 while we see one for NGC 1603. First, NGC 1601 might have a small transverse velocity; the tail would then be projected onto NGC 1601 along our line of sight. Additionally, the tail could be too faint, the projected velocity could be smaller than we estimated for NGC 1603, or projection effects could mean NGC 1601 is actually in a lower density region in the group gas than we calculate from the surface brightness profile and its projected radius.

5.3. Central X-ray Structure and Multi-Wavelength Comparisons

The X-ray emission near the center of the galaxy is elongated similarly to the optical emission (Figures 1 and 2). However, the details of the central X-ray structure are complex. Figures 7 and 8 display the excess emission immediately west of the galaxy center, as well as holes in the emission immediately north and south of the galaxy center.

One of the purposes of this *Chandra* observation was to compare the X-ray structure to the extended emission-line filaments and dust. In Figure 9, we display the H α +[N II] image (Trinchieri & di Serego Alighieri 1991) overlaid on the excess emission image of the inner $140 \times 140''$. The peak of the H α corresponds to excess emission west of the galaxy center; however, the detailed structure of the H α and excess X-ray emission do not have a one-to-one correspondence. Macchett et al. (1996) find $\sim 5 \times 5''$ of H α +[N II] emission centered on the optical center, with a slight north-south elongation. There is excess X-ray emission centered on the galaxy; however, a correlation of excess emission is made difficult by the possible presence of a central AGN and holes in the X-ray emission $\sim 2.5''$ to the north and south of the galaxy center.

On the left of Figure 10, we display the excess emission image of the inner $40 \times 40''$. It is overlaid by 4.885 GHz radio contours from Birkinshaw & Davies (1985). The double radio lobe structure is oriented in the north-south direction, and the lobe positions are roughly consistent with holes in the X-ray emission. Although the southern lobe's centroid is a bit offset from the hole, the $5''$ Gaussian smoothed image of H41 indicates that the lobe is cospatial with a region of softer emission. Considering the smoothing scale, this could be consistent with cool gas surrounding a radio bubble. No variation in H41 is observed near the northern lobe. These holes in X-ray emission may be due to the radio lobes, although this is uncertain.

In Figure 10, we also display a $V - R$ reddening map (Ferrari et al. 1999). The darker areas of the color index map correspond to regions of larger $V - R$ and extinction A_V . There is a clear filamentary structure to the west corresponding to a mean $A_V = 0.034 \pm 0.030$ (Ferrari et al. 1999), where the standard deviation is due to non-uniform extinction over the area of measurement. The optical extinction can be converted into a hydrogen column density assuming $N_H = 5.9 \times 10^{21} A_V / R_v \text{ cm}^{-2}$ (Spitzer 1978). Taking $R_V \equiv A_V / (B - V) = 3.2$, there is an excess N_H of $0.63 \pm 0.55 \times 10^{20} \text{ cm}^{-2}$ beyond the Galactic value of $4.86 \times 10^{20} \text{ cm}^{-2}$. If one assumes that the X-ray emission of a mekal model with $T = 0.85 \text{ keV}$ and solar abundance is absorbed by this extra column, the surface brightness would be reduced by only $\sim 2\%$ compared to that expected with no excess absorption. Of course, we actually observe an excess in the X-ray emission in this region of slightly larger extinction. The excess emission to the west of the galaxy is $\sim 1.5\text{--}2.5$ times the values expected from the surface brightness profile model.

Both the dust lanes and emission line filament appear to be cospatial in projection with the enhanced X-ray emission. There are several possible explanations for such a correlation. It might be that the hot and cool gas are in thermal contact, and that heat is being conducted from the hot gas to the cool gas (Sparks 1992). This might cool the X-ray gas; if it remained at nearly the same pressure due to the weight and pressure of the surrounding hot gas, the density and X-ray emissivity of the X-ray gas would increase. Mixing between the hot and cool gas could have a similar effect, as long as the X-ray gas didn't mix to a cool temperature out of the X-ray band. Third, the cool gas might result from radia-

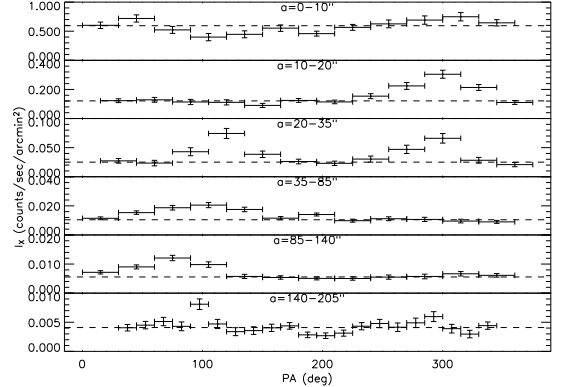


FIG. 8.— Surface brightness profiles, with 1σ error bars, of the unresolved emission (0.3–6 keV) as a function of PA for annuli with varying projected semi-major radii a . The dashed line indicates the best-fit constant surface brightnesses of each annulus, iteratively excluding PA regions more than 2σ from it. The last annuli excludes PA regions that extend beyond the S3 chip.

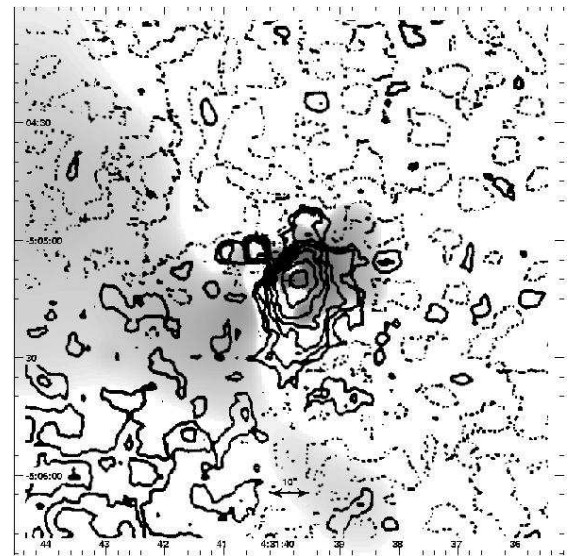


FIG. 9.— H α +[N II] contours (Trinchieri & di Serego Alighieri 1991) overlaid on adaptively smoothed image of unresolved X-ray emission ($140 \times 140''$) with a best-fit elliptical model for the surface brightness profile removed. The contours indicate line emission of $0, 1.7, 2, 4.1, 6.2, 8.3, 12.4, 18.6, 27.6, 41.4 \times 10^{-17} \text{ erg cm}^{-2} \text{ arcsec}^{-2}$. The cross indicates the center of the galaxy.

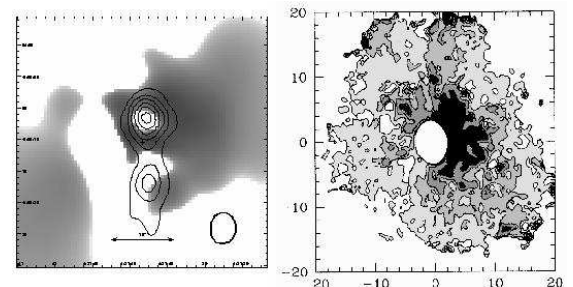


FIG. 10.— Left, adaptively smoothed gray scale image of unresolved X-ray emission ($40 \times 40''$) with the best-fit beta+power-law surface brightness profile removed. Contours are radio (4.885 GHz: 1, 2, 3, 4, 5, 6 mJy) with the beam in the lower-right corner (Birkinshaw & Davies 1985). The cross indicates the center of the galaxy. Right, gray scale image of $V - R$ ($0.625, 0.63, 0.635, 0.64$); the darker (redder in color) values in correspond to larger A_V (Ferrari et al. 1999).

tive cooling of X-ray gas. The cooling timescale at the center of NGC 1600 is on the order of 300 Myr, which is consistent with this explanation. On the other hand, it might be difficult to understand the presence of dust grains in cooled X-ray gas.

6. SPECTRAL ANALYSIS

We extracted spectra of the resolved sources and diffuse emission in NGC 1600, restricting analysis to the 0.7–9 keV range. The lower limit was taken to avoid calibration uncertainties, while there are few non-background counts beyond 9 keV. Since the telescope collecting area changes very rapidly near 2 keV and calibration problems led to poor fits in that spectral region, we chose to excise the 1.9–2.1 keV band when we fit line models (mekal). We do not find that this edge significantly affected fits of continuum models. All of the spectra were grouped to have at least 25 counts per spectral bin prior to background correction to enable our use of χ^2 statistics. In some cases, the fitted range of the spectra did not extend up to 9 keV because there were too few counts to form a bin up to this limiting energy.

The results of the spectral fits are summarized in Table 2. Spectra were extracted for the resolved point sources ('Sources') and the unresolved diffuse emission excluding the point sources ('Unresolved'). The third column gives the geometric region for the spectrum; 'Field' implies the entire S3 chip. The value of the absorbing column density (N_H) applied to all components of the model emission spectrum is given in column 4. In this and other columns, values in parentheses are fixed (not allowed to vary). The fixed value of N_H is the Galactic value from Dickey & Lockman (1990). To correct for the QE degradation, we used the XSPEC ACISABS model. Other elliptical galaxies are known to have both hard (point source) and soft (diffuse gas) components (Sarazin et al. 2001). Under the hard component, we fit three different models, thermal bremsstrahlung ('bremss'), power-law ('power'), and disk blackbody ('diskbb'). We always used the mekal model for the emission spectrum from hot diffuse gas. For the hard component, columns 5–7 give the spectral model(s), the temperature T_h (for bremsstrahlung or disk blackbody) or photon number spectral index Γ , and the unab-sorbed flux of the hard component(s), F_X^h (0.3–10 keV). Similarly, columns 8–10 give the temperature T_s , overall heavy element abundance relative to solar, and flux for the soft mekal component(s). For the unresolved emission, the spectra exclude regions around each of the $> 3\sigma$ flux determined resolved sources. The last two columns give the number of net counts in each spectrum, and χ^2 per dof for the best-fit model. All errors reported in the spectral analysis are 90% confidence level errors. Brackets are used when either the upper or lower bound on the confidence interval was unconstrained.

The background spectrum for the resolved sources were determined locally, using the same nearby regions as discussed in § 4. For the spectra of the unresolved emission, we used the deep blank sky backgrounds compiled by Maxim Markevitch².

The spectra of several spatial regions were analyzed. We have adopted the ellipticity and PA of the optical de Vaucouleurs fit. Some of the regions are scaled to the elliptical optical isophote containing one-half of the optical

light, the "one effective radius" region. In NGC 1600, the semi-major axis of this isophote, a_{eff} , is 55''.2. Since there were few source counts near the center of the galaxy, we fit the sources for the entire field. We searched for changes in unresolved emission with radius using annuli containing ~ 1000 net counts.

6.1. X-ray Spectrum of Resolved Sources

All resolved source spectral analysis was performed on sources with $> 3\sigma$ determined fluxes. Sources 1–3 were excluded because we are unsure that they are point sources. Sources 23 (NGC 1601), 40 (NGC 1603), and Source 50 (GSC 04742-00254) were also excluded because they are clearly not associated with NGC 1600. Since there are few source counts near the galaxy's center, we first extracted the cumulative spectrum of resolved sources within three effective radii, yielding only 372 net counts. This was insufficient to produce a well-constrained fit, so we chose to fit the sources in the entire field. The observed spectrum, containing 1318 net counts, is shown in Figure 11.

The combined spectrum of the sources was reasonably well-fit by either a thermal bremsstrahlung model with $kT_h = 4.73$ keV (Table 2, row 1) or power-law model with a photon number spectral index of $\Gamma = 1.76$ (row 3). The fits were not improved significantly when the absorbing column was allowed to vary (rows 2 and 4), so we fixed the hydrogen column at the Galactic value, $N_H = 4.86 \times 10^{20} \text{ cm}^{-2}$ (Dickey & Lockman 1990). Since the sources were very luminous, we also attempted a disk blackbody model; however, its χ^2 was worse by ~ 20 for the same number of dof. Finally, we attempted a disk blackbody + power-law spectral model ($kT_{\text{disk}} = 1.44$, $\Gamma = 1.95$, power-law responsible for $\sim 70\%$ of flux). This model had a χ^2 lower than our bremsstrahlung or power-law fits by ~ 2 ; however, the dof was also reduced by 2. Additionally, this fit had an unconstrained disk temperature, and poorly constrained power-law. We could have adopted either the bremsstrahlung or the power-law model for our best-fit. For comparison to other papers and since the power-law was constrained more tightly than the bremsstrahlung temperature, we adopted the power-law model as our best-fit. This model, including Galactic absorption and QE degradation, is shown in Figure 11 with the residuals to the fit. The power-law index is consistent with what was found from the hardness ratios. It is softer than the best-fit value of the sources simultaneously fit in a survey of 15 early-type galaxies (Irwin et al. 2003); however, it is consistent with both the spread of indices found when the galaxies are fit separately and the softer indices of the higher luminosity subsamples.

Approximately half of the sources in the entire field are expected to be foreground/background sources. On the other hand only ~ 1 is expected to be a foreground/background source within three effective radii. To ensure that unrelated sources do not heavily bias the spectral fits, we compared fits to the less constrained three effective radii spectrum with the fits to the entire field spectrum. Since all of the fits were consistent within the errors of the entire field spectrum fits, we do not believe the foreground/background sources heavily bias the spectral fits.

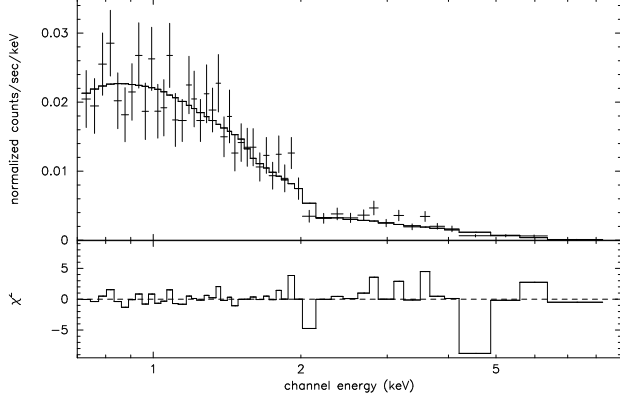


FIG. 11.— Upper panel: the cumulative X-ray spectrum of the resolved sources with $> 3\sigma$ detected flux in the entire field of NGC 1600. The spectrum has 1σ error bars and is overlaid by the solid histogram of the best-fit model spectrum (Table 2). Lower panel: the contribution to χ^2 with the sign indicating the sign of the residual.

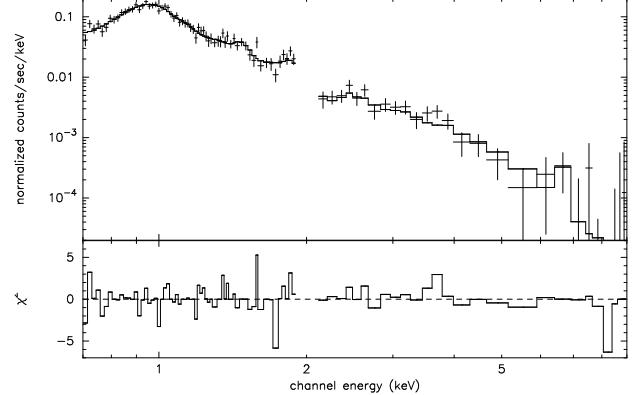


FIG. 12.— Upper panel, the cumulative X-ray spectrum of the unresolved emission within $1 a_{\text{eff}}$ of NGC 1600. The notation is the same as in Figure 11.

6.2. X-ray Spectra of Unresolved Emission

6.2.1. Projected Spectra

For the unresolved emission, the spectrum of the inner effective radius had 3662 net counts. This spectrum is shown in Figure 12. First, we attempted to model the unresolved emission with a soft mekal component representing the emission by diffuse interstellar gas (Table 2, row 11). The χ^2 was large, 168.6 for 87 dof. Since the unresolved emission includes unresolved point sources as well as diffuse gas, we added the adopted best-fit spectrum of the resolved sources to model the unresolved sources. The fit was much improved, $\chi^2 = 110.0$ for 86 dof; however, it was still rejected at the $> 95\%$ level. We allowed the absorbing column to vary, but this did not significantly improve the fit and was still consistent with the Galactic value. Therefore, we have assumed Galactic absorption for the remaining fits. Since the hardness ratios of the unresolved emission indicated spectral evolution at $a \sim 25''$, we attempted a two-temperature gas solution (row 9). We found a good fit, $\chi^2 = 78.7$ for 83 dof; however, the abundance of the low temperature gas was unconstrained. Therefore, we tried a two-temperature gas model with the abundances tied together. This fit, with a low mekal temperature of 0.85 ± 0.04 keV, a high mekal temperature of $2.55^{+0.52}_{-0.86}$ keV, and an abundance of $1.07^{+1.00}_{-0.40}$ solar, was almost as good as when both abundances were free. We also attempted a mekal cooling flow model; however, its fit, $\chi^2 = 94.4$ for 85 dof, was worse than the two-temperature model. Therefore, we adopted the two-temperature gas model (row 10) as our best-fit model for unresolved emission (Figure 12). Although the best-fit flux of this model from the unresolved point sources was not large, the upper limit on the flux of 1.41×10^{-13} erg cm $^{-2}$ s $^{-1}$ in 0.3–10 keV band still indicates unresolved sources could be a non-trivial source of emission in the inner effective radius.

Since this galaxy was bright enough to fit multiple annuli of unresolved emission, and there were indications of multiple temperatures of the diffuse gas, we attempted to determine the radial dependence of gas temperature

and abundance. We used eight annuli each with approximately 1000 net counts, out to $a = 180''$. In Table 2 rows 11–18, we show the results of assuming the model was the sum of the resolved point source model with its normalization free and a single temperature gas mekal model. Most of the fits produced reasonable χ^2 . Any radial changes in the abundance are dwarfed by the errors of the fits; although the best-fit abundances were mainly subsolar. On the other hand, it is clear that the first two annuli have a much lower temperature, ~ 0.85 keV, than the outer five annuli, ~ 1.5 keV. The temperature of the third annulus is intermediate between the two temperatures. These fits are in rough agreement with the two-temperature model found within one effective radius, $a < 55.2''$; however, the flux of the unresolved sources is smaller and the temperature fit for the hotter gas is larger when fitting the inner effective radius at once, as opposed to in multiple annuli. The best-fit normalization of the power-law and mekal model suggest that for $a < 180''$ they both contribute approximately equally to the flux. Within $1a_{\text{eff}}$, the diffuse gas is dominant by at least two-to-one. From the best-fit fluxes of the annular fits, we can estimate the X-ray luminosity (0.3–10 keV) to be $\sim 2.9 \times 10^{41}$ erg s $^{-1}$ in gas and $\sim 2.4 \times 10^{41}$ erg s $^{-1}$ in unresolved sources for $a < 180''$. Around 30–40% of the gaseous luminosity comes from the cooler gas. The resolved 3σ sources in the entire field have an X-ray luminosity of $\sim 1.4 \times 10^{41}$ erg s $^{-1}$. In $a < 180''$, this scales to $\sim 0.4 \times 10^{41}$ erg s $^{-1}$. Bolometric corrections increase the source luminosity by 44% and the total gaseous luminosity by 28%.

Using the RC3 optical profile, $a < 180''$ corresponds to $\sim 80\%$ of the total optical light, $L_{B,80\%} = 8.5 \times 10^{10} L_{B\odot}$ (O'Sullivan, Forbes, & Ponman 2001). The source X-ray-to-optical ratio is 3.3×10^{30} erg s $^{-1}$ $L_{B\odot}^{-1}$, approximately four times that found in NGC 4697 (Sarazin et al. 2001) or NGC 1553 (Blanton et al. 2001). It is more than ten times the expected contribution from discrete sources reported in O'Sullivan et al. (2001). Since the unresolved sources dominate the total source luminosity, there is an excess in the flux of faint sources in addition to the excess in the number of detected sources. It is unlikely that cosmic variance would lead to an excess number of sources at all fluxes. This suggests that the number of LMXBs

found in NGC 1600 is not proportional to the number of stars as estimated by the optical light, or that the unresolved source flux is overestimated. The most likely solution is that NGC 1600 has a high specific frequency of globular clusters; this is discussed in more detail later in the paper (See § 8).

The large unresolved hard component flux in the spectral models suggests that there are many unresolved point sources. This is also roughly consistent with the observed luminosity function for resolved sources (§ 4.3). If we extend the best-fit luminosity function down to 10^{36} erg s $^{-1}$ and adjust the normalizations to account for the observed sources within $3a_{\text{eff}}$, we expect an unresolved flux of $\sim 2.2 \times 10^{-13}$ erg cm $^{-2}$ s $^{-1}$ in the 0.3–10 keV band. Although this is approximately half of the flux estimated by the spectral fits, it is within the errors of the spectral fit flux. This agreement between the luminosity function and spectral fits could point to a large number of unresolved point sources. It might also suggest that there is no strong break in the luminosity function at lower X-ray luminosities than observed.

6.2.2. Deprojected Spectra

We also fit deprojected spectra. We did the deprojections by fitting the spectra from the outside annulus to the inside. Each annulus was fit assuming the best fit model for the emission in each of the outer annuli, and assuming simple geometric projection to include the emission from outer annuli in the inner ones. First, we allowed the power-law normalization and mekal model to vary within each annulus. The outer four annuli had unphysically large abundances, and in general the abundances were poorly constrained. The temperature results were similar to those for the projected fits. Next, we fit the deprojected spectra assuming a solar abundance in all annuli to ensure that the abundance problems in the previous deprojection did not cause problems in the temperature determination. This deprojection also produced results similar to the projected fits, except the jump between a low temperature gas and a high temperature gas moved inward. Since these results are qualitatively the same as the projected fit, but we had to assume a constant abundance, we choose not to present the details of these results.

6.2.3. Galaxy and Group Gas

Both the unresolved emission within one effective radius and the unresolved emission in annuli out to 180" point to a model involving two components of hot gas. In the inner 25–40" region, there is gas with $kT \sim 0.85$ keV. With a stellar velocity dispersion of 321 km s $^{-1}$ (Faber et al. 1989), NGC 1600 has a stellar kinetic temperature of ~ 0.65 keV, predicting an X-ray temperature of $\sim 1 \pm 0.2$ keV based on Davis & White (1996); Brown & Bregman (1998). This prediction is consistent with the measured X-ray temperature. At semi-major distances beyond 40", the gas is hotter, $kT \sim 1.5$ keV. This temperature is more consistent with the gas temperature of X-ray bright groups (Helsdon & Ponman 2000) than X-ray luminous early-type galaxies (O'Sullivan et al. 2003). Since the abundances are poorly constrained, we cannot tell if there is any gradient in the abundance, or if the average abundance is higher or lower than solar.

Near the same radius where there is a transition in spectrum, we saw transitions in the behavior of the surface brightness profile and the hardness ratios. This break in behavior of the surface brightness, hardness ratio, and spectrum at $a \sim 25$ –40" (7.3–11.7 kpc in projection) might be explained if emission from a lower temperature diffuse gas from the interstellar medium (ISM) of NGC 1600 dominates in the inner regions and a higher temperature diffuse gas from the intergalactic medium (IGM) of the NGC 1600 group provides the emission at larger radii.

The total gas X-ray-to-optical ratio is 3.4×10^{30} erg s $^{-1}$ L_B^{-1} ; the galaxy gas luminosity is ~ 30 –40% of the total gas luminosity. Compared to the $L_{X,\text{bol}}-L_B$ relationships from O'Sullivan et al. (2001), the galaxy and the total gaseous luminosity are consistent with the standard deviation around the best-fit relationship to the early-type galaxies excluding AGNs, brightest cluster galaxies and dwarfs. The total emission is consistent with the best-fit relationship for the brightest group galaxies.

7. MASS DETERMINATION

By combining the SBP model and the spectral fits of the diffuse gas, we estimated the gas and gravitational mass around NGC 1600. In eq. (3), the SBP is represented as the sum of two functions. Because the X-ray emissivity is a quadratic function of the density, eq. (3) does not lead to a simple expression for the gas density as the sum of two terms. Thus, we assumed that the two terms in the SBP represented two cospatial phases of gas, a 0.85 keV gas following the inner beta model profile and a 1.5 keV gas following the outer beta model profile. To remove the $\sim 30\%$ contribution to the counts by unresolved point sources (See § 5), we multiplied the SBP by 0.7. We integrated the sum of the physical densities over volume to determine the gas mass, and we used hydrostatic equilibrium to estimate the gravitational mass. For both estimates, we assumed the galaxy was shaped as an oblate spheroid.

In Figure 13, we display the resulting gravitational and gas mass profiles. At $a \sim 20"$, there is a slope change in the gravitational mass profile. This indicates the likely presence of two gravitational potentials, supporting the view that the exterior gas is group gas and the interior

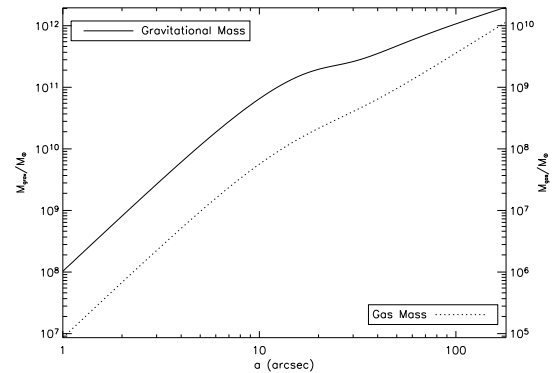


FIG. 13.— The estimated gas and gravitational mass profiles around NGC 1600. The dotted line and right axis display the gas mass profile, while the solid line and left axis display the gravitational mass profile.

gas is galaxy gas. On the other hand, the total gravitational mass within $a < 180''$ is only $2.0 \pm 0.5 \times 10^{12} M_{\odot}$ with errors in the hot gas temperature dominating the error budget. The mass-to-light ratio for $a < 180''$ is $M/L_B = (24 \pm 6) M_{\odot}/L_{B\odot}$. Within one effective radius, the mass-to-light ratio is $(10 \pm 3) M_{\odot}/L_{B\odot}$. The total mass is not that much larger than might be expected for NGC 1600 alone, which may not be consistent with the suggestion that the outer component is due to a group dark matter potential.

The total gas mass within $a < 180''$ is $1.14 \pm 0.06 \times 10^{10} M_{\odot}$, with errors in the surface brightness dominating the error budget. Assuming a normal elliptical galaxy stellar mass loss rate per stellar luminosity of $1.3 \times 10^{-11} M_{\odot}/L_{B\odot}$ (Mathews & Brighten 2003), the rate of stellar mass loss for the entire galaxy is about $1.4 M_{\odot} \text{ yr}^{-1}$. Almost all of the gas mass around NGC 1600 can be attributed to stellar mass loss in NGC 1600, assuming an age of 7.3 Gyr (Terlevich & Forbes 2002). This is not surprising since NGC 1600 dominates the stellar population of the NGC 1600 group. On the other hand, it is not consistent with a large amount of intergalactic group gas in the system.

8. CONCLUSIONS

We have used *Chandra* observations to study the X-ray emission from the point sources and unresolved emission of NGC 1600. Since NGC 1600 is ~ 60 Mpc away, we could only resolve the very brightest point sources. We detected 71 total point sources, of which 45 were bright enough to have fluxes determined at $\geq 3\sigma$. We identified two of the sources with foreground stars, two with known galaxy members of the NGC 1600 group, and three with non-stellar objects, presumably galaxies. We did not clearly detect a point source at the center of NGC 1600, and we put a conservative 0.3–10 keV upper flux limit of $6.7 \times 10^{39} \text{ erg s}^{-1}$ on the luminosity of the central AGN.

Twenty-one of the sources without clear associations to objects besides NGC 1600 are brighter than $2 \times 10^{39} \text{ erg s}^{-1}$ (0.3–10 keV); approximately 11 ± 2 of those sources are expected to be unrelated foreground/background sources. The excess is strongest within two D25, where we observe a source density of $2250 \pm 796 \text{ deg}^{-2}$ compared to the expected $600 \pm 100 \text{ deg}^{-2}$. NGC 1600 may have the largest number of ULX candidates observed to date in an early-type galaxy, although cosmic variance in the background source population cannot be completely ruled out. A combination of cosmic variance for the high flux sources and a distance overestimate of $\sim 40\%$ could also reduce the number of ULX candidates; however, this model requires NGC 1600 have a peculiar velocity of $\sim +1300 \text{ km s}^{-1}$. As found in Irwin et al. (2003), the bright LMXBs have softer spectra than is typical for fainter LMXBs in early-type galaxies. The spectrum of sources in NGC 1600, $\Gamma = 1.76^{+0.10}_{-0.09}$, and the luminosity function slope, $\alpha = 2.00^{+1.14}_{-0.35}$, both suggest that these sources are different than ULX candidates observed in star-forming galaxies. The age of the galaxy and the X-ray spectra of the sources argue against these sources being HMXBs.

Since this galaxy is X-ray bright, we expected the unresolved emission to dominate the flux. Although this

is true, the contribution from unresolved point sources is nearly as large as that due to the diffuse gas in the best-fit models. Even if one uses the lower limit on the unresolved point source flux, unresolved point sources are responsible for $\gtrsim 25\%$ of the unresolved flux. Combined with the large normalization of the X-ray luminosity function, this suggests that NGC 1600 has a larger population of LMXBs than found in most previously observed galaxies (Sarazin et al. 2001; Blanton et al. 2001; Finoguenov & Jones 2002; Zezas & Fabbiano 2002; Jeltema et al. 2003; Sivakoff et al. 2003; Randall et al. 2004). When normalized to the optical luminosity of the galaxy, the source X-ray-to-optical ratio is also very high, $L_X/L_B = 3.3 \times 10^{30} \text{ erg s}^{-1} L_{B\odot}^{-1}$. This ratio is a factor of two larger than found in most early-type galaxies. Recently, Gilfanov (2004) suggested that total X-ray source luminosities correlate better with near-infrared luminosities than with optical luminosities. From the extrapolated 2MASS K_s magnitude (8.04), $M_{K_s,\odot} = 3.39$, and the distance of NGC 1600, we find that the source X-ray-to-near-infrared ratio is almost an order of magnitude higher than the average found in Gilfanov (2004). Gilfanov (2004) limited the sources he considered in his total X-ray luminosities to $L_X > 10^{37} \text{ erg s}^{-1}$, so part of the difference might be explained if NGC 1600 has a very large number of fainter sources.

Previous studies have shown that a large fraction of LMXBs in elliptical galaxies are located in globular clusters (Sarazin et al. 2000, 2001; Angelini et al. 2001; Kundu et al. 2003; Sarazin et al. 2003), and that the luminosity of LMXBs may correlate better with the GC population than the optical luminosity (White et al. 2002; Sarazin et al. 2003). Unfortunately, we were unable to find a determination of the GC population in NGC 1600, which is more distant than most galaxies which have GC observations. However, one explanation for the large number of LMXBs in NGC 1600 would be that this galaxy has a large GC specific frequency. Thus, we predict that NGC 1600 will be found to have large numbers of GCs. Observations of the GC population in NGC 1600 would be very useful to test this prediction. Such a large population of GCs might be connected to NGC 1600's position as the central elliptical galaxy in a group with a significant potential; it may be more closely related to cD galaxies, which have larger GC populations (e.g., Harris 1991) than normal ellipticals.

We note that many of the bright X-ray sources associated with NGC 1600 are at large distances from the galaxy center. One possibility is that these sources are due to cosmic variance in the background source population. For the sources within two D25, the variance would have to be much larger than the $\sim 8\%$ cosmic variance between the Chandra Deep Fields found by (Rosati et al. 2002). Another possibility is that these sources are actually located in intergalactic GCs in the NGC 1600 group, rather than being directly associated with NGC 1600. Recently, intergalactic GCs have probably been detected in nearby groups and clusters (e.g., Bassino et al. 2003).

The X-ray image, surface brightness profile, and spatially resolved spectra suggest that there are two components to the gas around NGC 1600. There is a component which is centered on NGC 1600, which has a small spatial scale ($\lesssim 25''$) and a lower temperature (0.85 keV), which we propose is gas which is bound to NGC 1600. A second

component is centered to the northeast of NGC 1600, has a larger spatial scale, and is hotter (1.5 keV); we argue that this gas is bound to the dark matter potential of the NGC 1600 group. The X-ray image suggests that the center of the potential of the group is slightly displaced from the center of NGC 1600. One would expect that NGC 1600 would be moving in the group potential, and this motion could affect the distribution of the galaxy and group gas.

We also observe structure to the diffuse emission on small scales. Excess emission is seen west of the center of NGC 1600 in the inner 35''. This excess emission is partially cospatial with H α and dust filaments. Possible models to explain this correlation of hot and cooler gas include thermal conduction between the two phases, radiative cooling of the hot X-ray gas to form the cooler gas, and mixing of the hot and cool gas. Directly to the north and south of the galaxy center, there are holes in the X-ray emission. These holes are roughly coincident with the lobes of the radio source, suggesting that there may be two radio bubbles being blown in the hot gas. Finally, we see that NGC 1603, a galaxy east of NGC 1600, has a tail of soft X-ray emission to its west. Calculations

indicate that this is likely to be a ram-pressure stripped tail of ISM from NGC 1603, removed as a result of motions of this galaxy through the surrounding group gas.

Support for this work was provided by the National Aeronautics and Space Administration through *Chandra* Award Numbers GO2-3100X, GO2-3099X, GO3-4099X, AR3-4005X, GO4-5093X, and AR4-5008X, issued by the *Chandra* X-ray Observatory Center, which is operated by the Smithsonian Astrophysical Observatory for and on behalf of NASA under contract NAS8-39073. GRS acknowledges the receipt of an Achievement Reward for College Scientists fellowship. Partial support was also provided by the Celerity Foundation. This research has made use of the NASA/IPAC Extragalactic Database (NED) which is operated by the Jet Propulsion Laboratory, California Institute of Technology, under contract with the National Aeronautics and Space Administration, the SIMBAD database, operated at CDS, Strasbourg, France, and the Digitized Sky Surveys, produced at the Space Telescope Science Institute under U.S. Government grant NAG W-2166.

REFERENCES

Angelini, L., Loewenstein, M., & Mushotzky, R. F. 2001, ApJ, 557, L35

Bassino, L. P., Cellone, S. A., Forte, J. C., & Dirsch, B. 2003, A&A, 399, 489

Begelman, M. C. 2002, ApJ, 568, L97

Birkinshaw, M., & Davies, R. L. 1985, ApJ, 291, 32

Blanton, E. L., Sarazin, C. L., & Irwin, J. A. 2001, ApJ, 552, 106

Brandt, W. N., et al. 2000, AJ, 119, 2349

—. 2001, AJ, 122, 2810

Brown, B. A., & Bregman, J. N. 1998, ApJ, 495, L75+

Colbert, E. J. M., & Mushotzky, R. F. 1999, ApJ, 519, 89

Condon, J. J., & Broderick, J. J. 1991, AJ, 102, 1663

Davis, D. S., & White, R. E. 1996, ApJ, 470, L35+

de Vaucouleurs, G., de Vaucouleurs, A., Corwin, H. G., Buta, R. J., Paturel, G., & Fouque, P. 1992, Third Reference Catalogue of Bright Galaxies (RC3)

Dickey, J. M., & Lockman, F. J. 1990, ARA&A, 28, 215

Fabbiano, G. 1989, ARA&A, 27, 87

Fabbiano, G., Kim, D.-W., & Trinchieri, G. 1994, ApJ, 429, 94

Faber, S. M., & Burstein, D. 1988, in Large-Scale Motions in the Universe: A Vatican study Week, 115–167

Faber, S. M., Wegner, G., Burstein, D., Davies, R. L., Dressler, A., Lynden-Bell, D., & Terlevich, R. J. 1989, ApJS, 69, 763

Ferrari, F., Pastoriza, M. G., Macchetto, F., & Caon, N. 1999, A&AS, 136, 269

Finoguenov, A., & Jones, C. 2002, ApJ, 574, 754

Forman, W., Jones, C., & Tucker, W. 1985, ApJ, 293, 102

Frogel, J. A., Persson, S. E., Matthews, K., & Aaronson, M. 1978, ApJ, 220, 75

Fryer, C. L., & Kalogera, V. 2001, ApJ, 554, 548

Gehrels, N. 1986, ApJ, 303, 336

Giacconi, R., et al. 2001, ApJ, 551, 624

Gilfanov, M. 2004, MNRAS, 349, 146

Grindlay, J. E. 1984, Advances in Space Research, 3, 19

Harris, W. E. 1991, ARA&A, 29, 543

Helsdon, S. F., & Ponman, T. J. 2000, MNRAS, 315, 356

Hög, E., et al. 2000, A&A, 355, L27

Irwin, J. A., Athey, A. E., & Bregman, J. N. 2003, ApJ, 587, 356

Irwin, J. A., Bregman, J. N., & Athey, A. E. 2004, ApJ, 601, L143

Irwin, J. A., Sarazin, C. L., & Bregman, J. N. 2002, ApJ, 570, 152

Jeltema, T. E., Canizares, C. R., Buote, D. A., & Garmire, G. P. 2003, ApJ, 585, 756

Kim, D., & Fabbiano, G. 2003, ApJ, 586, 826

Kim, D.-W., Fabbiano, G., Matsumoto, H., Koyama, K., & Trinchieri, G. 1996, ApJ, 468, 175

King, A. R. 2002, MNRAS, 335, L13

King, A. R., Davies, M. B., Ward, M. J., Fabbiano, G., & Elvis, M. 2001, ApJ, 552, L109

Kundu, A., Maccarone, T. J., Zepf, S. E., & Puzia, T. H. 2003, ApJ, 589, L81

Macchetto, F., Pastoriza, M., Caon, N., Sparks, W. B., Giavalisco, M., Bender, R., & Capaccioli, M. 1996, A&AS, 120, 463

Makishima, K., et al. 2000, ApJ, 535, 632

Mathews, W. G., & Brighenti, F. 2003, ARA&A, 41, 191

Matthias, M., & Gerhard, O. 1999, MNRAS, 310, 879

Miller, M. C., & Hamilton, D. P. 2002, MNRAS, 330, 232

Monet, D. G., et al. 2003, AJ, 125, 984

Mushotzky, R. F., Cowie, L. L., Barger, A. J., & Arnaud, K. A. 2000, Nature, 404, 459

O'Sullivan, E., Forbes, D. A., & Ponman, T. J. 2001, MNRAS, 328, 461

O'Sullivan, E., Ponman, T. J., & Collins, R. S. 2003, MNRAS, 340, 1375

Pellegrini, S. 1994, A&A, 292, 395

Prugniel, P., & Simien, F. 1996, A&A, 309, 749

Randall, S. W., Sarazin, C. L., & Irwin, J. A. 2004, ApJ, accepted

Rembold, S. B., Pastoriza, M. G., Ducati, J. R., Rubio, M., & Roth, M. 2002, A&A, 391, 531

Rosati, P., et al. 2002, ApJ, 566, 667

Sandage, A. 1973, ApJ, 183, 711

Sarazin, C. L., Irwin, J. A., & Bregman, J. N. 2000, ApJ, 544, L101

—. 2001, ApJ, 556, 533

Sarazin, C. L., Kundu, A., Irwin, J. A., Sivakoff, G. R., Blanton, E. L., & Randall, S. W. 2003, ApJ, 595, 743

Sivakoff, G. R., Sarazin, C. L., & Irwin, J. A. 2003, ApJ, 0, 0

Sparks, W. B. 1992, ApJ, 399, 66

Spitzer, L. 1978, Physical processes in the interstellar medium (New York Wiley-Interscience, 1978, 333 p.)

Terlevich, A. I., & Forbes, D. A. 2002, MNRAS, 330, 547

Tonry, J. L., Dressler, A., Blakeslee, J. P., Ajhar, E. A., Fletcher, A. B., Luppino, G. A., Metzger, M. R., & Moore, C. B. 2001, ApJ, 546, 681

Trager, S. C., Faber, S. M., Worthey, G., & González, J. J. 2000, AJ, 119, 1645

Trinchieri, G., & di Serego Alighieri, S. 1991, AJ, 101, 1647

Trinchieri, G., Fabbiano, G., & Canizares, C. R. 1986, ApJ, 310, 637

White, R. E., Sarazin, C. L., & Kulkarni, S. R. 2002, ApJ, 571, L23

Zezas, A., & Fabbiano, G. 2002, ApJ, 577, 726

TABLE 1
DISCRETE X-RAY SOURCES IN NGC 1600

Src. No. (1)	Name (2)	R.A. (h m s) (3)	Dec. (° ' '') (4)	<i>d</i> ('') (5)	<i>a</i> ('') (6)	Count Rate (10^{-4} s $^{-1}$) (7)	S/N (8)	L_X (9)	H21 0 (10)	H31 0 (11)	H32 0 (12)	Notes (13)
1	CXOU J043139.8-050511	04 31 39.88	-05 05 11.4	0.9	1.0	38.91 \pm 3.10	12.55	160.3	-0.50 $^{+0.11}_{-0.09}$	-0.96 $^{+0.09}_{-0.03}$	-0.88 $^{+0.22}_{-0.08}$	a,b,d,e
2	CXOU J043140.0-050504	04 31 40.05	-05 05 04.7	6.4	6.5	15.00 \pm 1.94	7.75	61.8	-0.29 $^{+0.25}_{-0.21}$	-0.88 $^{+0.24}_{-0.09}$	-0.78 $^{+0.36}_{-0.15}$	a,b
3	CXOU J043139.7-050456	04 31 39.71	-05 04 56.6	14.1	15.5	7.31 \pm 1.42	5.16	30.1	-0.48 $^{+0.28}_{-0.21}$	-0.91 $^{+0.43}_{-0.09}$	-0.77 $^{+0.77}_{-0.20}$	a,b
4	CXOU J043138.1-050456	04 31 38.15	-05 04 56.9	29.0	42.3	1.78 \pm 0.70	2.55	7.3	-0.80 $^{+1.09}_{-0.19}$	-0.67 $^{+0.63}_{-0.25}$	+0.27 $^{+0.67}_{-1.11}$...
5	CXOU J043140.1-050540	04 31 40.15	-05 05 40.7	30.6	33.2	4.26 \pm 1.05	4.05	17.5	-0.78 $^{+0.66}_{-0.18}$	-0.48 $^{+0.36}_{-0.25}$	+0.47 $^{+0.42}_{-0.87}$...
6	CXOU J043139.7-050436	04 31 39.75	-05 04 36.3	34.2	36.1	1.55 \pm 0.65	2.37	6.4	+0.62 $^{+0.36}_{-1.41}$	-0.22 $^{+1.18}_{-0.76}$	-0.74 $^{+0.98}_{-0.23}$	e
7	CXOU J043138.3-050536	04 31 38.30	-05 05 36.7	35.2	39.2	7.48 \pm 1.35	5.52	30.8	+0.30 $^{+0.53}_{-0.32}$	+0.12 $^{+0.35}_{-0.42}$	-0.18 $^{+0.44}_{-0.22}$...
8	CXOU J043141.2-050543	04 31 41.23	-05 05 43.0	38.4	49.1	4.77 \pm 1.10	4.33	19.7	-0.42 $^{+0.34}_{-0.25}$	-0.67 $^{+0.34}_{-0.19}$	-0.35 $^{+0.47}_{-0.34}$	e
9	CXOU J043137.3-050457	04 31 37.33	-05 04 57.2	40.2	59.4	3.48 \pm 0.93	3.73	14.3	-0.26 $^{+0.41}_{-0.34}$	-0.67 $^{+0.50}_{-0.23}$	-0.50 $^{+0.57}_{-0.33}$...
10	CXOU J043139.8-050552	04 31 39.84	-05 05 52.3	41.9	43.4	8.32 \pm 1.42	5.87	34.3	-0.72 $^{+0.17}_{-0.11}$	-0.86 $^{+0.17}_{-0.08}$	-0.39 $^{+0.48}_{-0.33}$	f
11	CXOU J043137.3-050536	04 31 37.31	-05 05 36.0	46.0	56.6	1.43 \pm 0.61	2.36	5.9	-0.72 $^{+1.05}_{-0.25}$	-0.50 $^{+0.75}_{-0.37}$	+0.35 $^{+0.59}_{-1.09}$...
12	CXOU J043141.9-050550	04 31 41.99	-05 05 50.8	51.3	68.0	2.03 \pm 0.73	2.78	8.4	+0.25 $^{+0.50}_{-0.68}$	-0.65 $^{+1.16}_{-0.32}$	-0.78 $^{+0.93}_{-0.20}$...
13	CXOU J043141.5-050421	04 31 41.50	-05 04 21.0	55.1	56.3	1.52 \pm 0.63	2.40	6.3	+0.06 $^{+0.62}_{-0.66}$	-1.00 $^{+0.66}_{-0.00}$	-1.00 $^{+0.00}_{-0.48}$	e
14	CXOU J043139.8-050407	04 31 39.81	-05 04 07.1	63.4	66.1	3.65 \pm 0.94	3.90	15.0	-0.15 $^{+0.42}_{-0.37}$	-0.53 $^{+0.49}_{-0.29}$	-0.40 $^{+0.33}_{-0.33}$...
15	CXOU J043136.0-050542	04 31 36.04	-05 05 42.2	65.5	83.2	1.66 \pm 0.65	2.56	6.9	-0.27 $^{+0.91}_{-0.60}$	+0.01 $^{+0.71}_{-0.72}$	+0.28 $^{+0.51}_{-0.73}$...
16	CXOU J043135.1-050502	04 31 35.17	-05 05 02.6	70.7	103.9	9.47 \pm 1.51	6.26	39.0	-0.25 $^{+0.22}_{-0.20}$	-0.61 $^{+0.23}_{-0.16}$	-0.43 $^{+0.27}_{-0.21}$	f
17	CXOU J043143.2-050411	04 31 43.27	-05 04 11.3	78.0	86.3	5.49 \pm 1.18	4.63	22.6	-0.48 $^{+0.24}_{-0.18}$	-1.00 $^{+0.12}_{-0.00}$	-1.00 $^{+0.33}_{-0.00}$	f
18	CXOU J043145.0-050511	04 31 45.09	-05 05 11.1	78.0	113.5	1.66 \pm 0.65	2.54	6.8	-0.47 $^{+0.34}_{-0.37}$	-0.81 $^{+0.91}_{-0.17}$	-0.54 $^{+1.12}_{-0.41}$	d
19	CXOU J043145.0-050438	04 31 45.06	-05 04 38.1	84.0	111.0	1.24 \pm 0.56	2.20	5.1	-0.35 $^{+0.77}_{-0.51}$	-0.40 $^{+0.88}_{-0.70}$	-0.06 $^{+0.77}_{-0.51}$...
20	CXOU J043139.9-050339	04 31 39.93	-05 03 39.2	91.3	94.6	1.48 \pm 0.60	2.45	6.1	-0.02 $^{+0.89}_{-0.86}$	+0.26 $^{+0.45}_{-1.00}$	+0.28 $^{+0.51}_{-0.73}$...
21	CXOU J043134.2-050431	04 31 34.25	-05 04 31.1	92.7	136.0	5.54 \pm 1.15	4.82	22.8	-0.72 $^{+0.22}_{-0.13}$	-0.95 $^{+0.36}_{-0.04}$	-0.73 $^{+1.00}_{-0.24}$	f
22	CXOU J043143.6-050627	04 31 43.65	-05 06 27.6	95.6	125.5	3.75 \pm 0.97	3.85	15.5	+0.16 $^{+0.54}_{-0.65}$	+0.04 $^{+0.59}_{-0.62}$	-0.11 $^{+0.40}_{-0.37}$...
23	CXOU J043141.7-050336	04 31 41.78	-05 03 36.9	97.9	97.9	2.73 \pm 0.83	3.30	11.2	-0.47 $^{+0.67}_{-0.67}$	-0.60 $^{+0.69}_{-0.30}$	-0.18 $^{+0.75}_{-0.59}$	d
24	CXOU J043141.2-050654	04 31 41.25	-05 06 54.3	105.8	117.5	2.80 \pm 0.82	3.43	11.5	+0.01 $^{+0.81}_{-0.61}$	-0.16 $^{+0.69}_{-0.56}$	-0.17 $^{+0.51}_{-0.43}$	e
25	CXOU J043141.6-050653	04 31 41.61	-05 06 53.5	106.3	120.4	12.63 \pm 1.71	7.38	52.0	+0.41 $^{+0.55}_{-0.34}$	+0.36 $^{+0.27}_{-0.34}$	-0.05 $^{+0.17}_{-0.17}$	f
26	CXOU J043132.6-050513	04 31 32.61	-05 05 13.1	108.5	156.9	1.52 \pm 0.62	2.46	6.3	-0.61 $^{+0.83}_{-0.32}$	-0.59 $^{+0.73}_{-0.31}$	+0.03 $^{+0.76}_{-0.80}$...
27	CXOU J043139.5-050711	04 31 39.58	-05 07 11.5	121.1	124.6	16.02 \pm 1.92	8.32	66.0	-0.29 $^{+0.16}_{-0.15}$	-0.52 $^{+0.16}_{-0.13}$	-0.27 $^{+0.18}_{-0.17}$	f
28	CXOU J043132.1-050428	04 31 32.13	-05 04 28.6	123.0	181.5	3.31 \pm 0.89	3.71	13.6	-0.46 $^{+0.33}_{-0.24}$	-0.83 $^{+0.38}_{-0.13}$	-0.60 $^{+0.63}_{-0.29}$...
29	CXOU J043144.8-050331	04 31 44.80	-05 03 31.9	123.1	132.8	11.38 \pm 1.64	6.92	46.9	-0.22 $^{+0.19}_{-0.17}$	-0.68 $^{+0.19}_{-0.13}$	-0.54 $^{+0.22}_{-0.17}$	f
30	CXOU J043132.2-050422	04 31 32.25	-05 04 22.6	123.5	181.7	13.46 \pm 1.82	7.38	55.4	+0.30 $^{+0.24}_{-0.28}$	+0.05 $^{+0.29}_{-0.30}$	-0.26 $^{+0.18}_{-0.16}$	e,f
31	CXOU J043147.5-050612	04 31 47.55	-05 06 12.6	130.5	190.2	0.68 \pm 0.43	1.56	2.8	-1.00 $^{+0.60}_{-0.00}$	-1.00 $^{+0.44}_{-0.44}$	+0.00 $^{+1.00}_{-1.00}$...
32	CXOU J043147.1-050353	04 31 47.18	-05 03 53.5	133.6	163.0	3.34 \pm 0.91	3.69	13.8	-0.16 $^{+0.48}_{-0.42}$	-0.31 $^{+0.51}_{-0.38}$	-0.15 $^{+0.44}_{-0.39}$...
33	CXOU J043136.1-050308	04 31 36.19	-05 03 08.3	133.9	162.7	1.71 \pm 0.65	2.65	7.1	-0.52 $^{+0.63}_{-0.63}$	-0.81 $^{+0.91}_{-0.17}$	-0.50 $^{+1.13}_{-0.45}$	d
34	CXOU J043146.4-050338	04 31 46.48	-05 03 38.4	135.1	156.1	2.00 \pm 0.71	2.83	8.2	-0.43 $^{+0.59}_{-0.37}$	-0.81 $^{+0.91}_{-0.17}$	-0.58 $^{+1.11}_{-0.38}$...
35	CXOU J043142.2-050257	04 31 42.24	-05 02 57.2	137.8	137.8	1.26 \pm 0.56	2.25	5.2	+0.31 $^{+0.60}_{-1.03}$	-0.40 $^{+1.24}_{-0.56}$	-0.64 $^{+1.08}_{-0.33}$...
36	CXOU J043131.3-050411	04 31 31.34	-05 04 11.8	140.2	205.8	2.97 \pm 0.87	3.40	12.2	-0.59 $^{+0.40}_{-0.32}$	-0.96 $^{+1.88}_{-0.04}$	-0.86 $^{+1.84}_{-0.44}$...
37	CXOU J043141.8-050252	04 31 41.84	-05 02 52.5	141.1	141.3	1.93 \pm 0.68	2.82	8.0	+0.41 $^{+0.77}_{-0.29}$	+0.40 $^{+0.53}_{-1.28}$	-0.01 $^{+0.55}_{-0.57}$...
38	CXOU J043148.6-050415	04 31 48.60	-05 04 15.9	141.5	186.8	1.33 \pm 0.59	2.27	5.5	-0.35 $^{+0.87}_{-0.51}$	-0.40 $^{+0.88}_{-0.47}$	-0.06 $^{+0.77}_{-0.70}$...
39	CXOU J043138.2-050245	04 31 38.21	-05 02 45.4	147.2	161.8	1.25 \pm 0.56	2.23	5.2	+0.57 $^{+1.39}_{-1.39}$	-1.00 $^{+2.00}_{-0.00}$	-1.00 $^{+0.55}_{-0.00}$...
40	CXOU J043149.8-050539	04 31 49.86	-05 05 39.7	152.2	224.8	3.16 \pm 0.87	3.62	13.0	-1.00 $^{+0.51}_{-0.00}$	-0.67 $^{+0.57}_{-0.24}$	+1.00 $^{+0.00}_{-2.00}$	d
41	CXOU J043147.0-050308	04 31 47.07	-05 03 08.7	162.5	180.7	2.88 \pm 0.84	3.45	11.9	-0.16 $^{+0.48}_{-0.42}$	-0.52 $^{+0.58}_{-0.32}$	-0.39 $^{+0.55}_{-0.37}$...
42	CXOU J043132.2-050712	04 31 32.25	-05 07 12.0	166.6	187.2	4.88 \pm 1.13	4.31	20.1	+1.00 $^{+0.60}_{-1.21}$	+1.00 $^{+0.60}_{-0.64}$	+0.22 $^{+0.30}_{-0.35}$	f
43	CXOU J043148.8-050328	04 31 48.83	-05 03 28.1	168.5	202.3	1.10 \pm 0.52	2.09	4.5	-0.35 $^{+0.61}_{-0.61}$	+0.12 $^{+0.76}_{-0.93}$	+0.45 $^{+0.99}_{-1.10}$...
44	CXOU J043146.0-050735	04 31 46.08	-05 07 35.7	172.4	221.3	1.30 \pm 0.60	2.16	5.3	-0.21 $^{+0.67}_{-0.52}$	-1.00 $^{+0.21}_{-0.00}$	-1.00 $^{+0.31}_{-0.00}$...
45	CXOU J043135.5-050222	04 31 35.50	-05 02 22.7	180.0	214.2	1.76 \pm 0.67	2.65	7.30	+0.46 $^{+0.47}_{-1.07}$	-0.40 $^{+1.24}_{-0.56}$	-0.73 $^{+1.00}_{-0.24}$...
46	CXOU J043127.8-050537	04 31 27.82	-05 05 37.5	182.0	257.3	6.80 \pm 1.29	5.28	28.0	-0.04 $^{+0.36}_{-0.36}$	-0.04 $^{+0.36}_{-0.35}$	-0.00 $^{+0.28}_{-0.28}$	f
47	CXOU J043142.9-050213	04 31 42.98	-05 02 13.3	183.2	183.2	1.90 \pm 0.89	2.14	7.8	+1.00 $^{+0.00}_{-2.00}$	+1.00 $^{+0.00}_{-2.00}$	-0.26 $^{+0.77}_{-0.54}$	c

TABLE 1 — *Continued*

Src. No. (1)	Name (2)	R.A. (h m s) (3)	Dec. (° ' '') (4)	<i>d</i> ('') (5)	<i>a</i> ('') (6)	Count Rate (10^{-4} s $^{-1}$) (7)	S/N (8)	L_X (9)	$H21^0$ (10)	$H31^0$ (11)	$H32^0$ (12)	Notes (13)
48	CXOU J043137.8–050818	04 31 37.80	–05 08 18.3	190.4	191.5	3.12±0.89	3.53	12.9	–0.65 $^{+0.50}_{-0.24}$	–0.74 $^{+0.50}_{-0.19}$	–0.18 $^{+0.75}_{-0.59}$...
49	CXOU J043127.7–050405	04 31 27.75	–05 04 05.9	192.2	283.9	1.91±0.69	2.77	7.93	+0.21 $^{+0.53}_{-0.68}$	–0.28 $^{+0.80}_{-0.54}$	–0.46 $^{+0.59}_{-0.35}$	e
50	CXOU J043130.4–050256	04 31 30.44	–05 02 56.1	194.6	269.3	75.83±4.18	18.14	312.4	–0.78 $^{+0.03}_{-0.03}$	–0.99 $^{+0.02}_{-0.01}$	–0.92 $^{+0.12}_{-0.05}$	d
51	CXOU J043150.1–050304	04 31 50.16	–05 03 04.7	198.7	235.5	23.13±2.34	9.90	95.3	–0.54 $^{+0.10}_{-0.09}$	–0.77 $^{+0.09}_{-0.07}$	–0.39 $^{+0.18}_{-0.16}$	f
52	CXOU J043134.2–050205	04 31 34.21	–05 02 05.2	203.7	247.9	5.99±2.74	2.21	24.7	+1.00 $^{+2.00}_{-0.00}$	+1.00 $^{+2.00}_{-0.00}$	+0.56 $^{+1.09}_{-0.05}$	c
53	CXOU J043147.4–050212	04 31 47.45	–05 02 12.5	210.9	221.9	116.05±7.08	16.41	478.1	–0.41 $^{+0.06}_{-0.06}$	–0.76 $^{+0.05}_{-0.04}$	–0.50 $^{+0.08}_{-0.08}$	c,f
54	CXOU J043134.6–050826	04 31 34.68	–05 08 26.8	211.0	212.6	4.45±1.10	4.05	18.3	+0.04 $^{+0.38}_{-0.40}$	–0.65 $^{+0.58}_{-0.25}$	–0.67 $^{+0.50}_{-0.23}$...
55	CXOU J043153.6–050408	04 31 53.68	–05 04 08.6	215.4	293.8	26.29±2.64	9.94	108.3	–0.26 $^{+0.13}_{-0.12}$	–0.61 $^{+0.12}_{-0.10}$	–0.42 $^{+0.15}_{-0.13}$	f
56	CXOU J043150.9–050730	04 31 50.96	–05 07 30.7	217.1	304.9	2.77±0.86	3.24	11.4	–0.13 $^{+0.47}_{-0.47}$	–0.72 $^{+0.73}_{-0.62}$	–0.65 $^{+0.73}_{-0.27}$...
57	CXOU J043125.4–050540	04 31 25.43	–05 05 40.6	217.8	308.5	4.11±1.04	3.96	17.0	–0.04 $^{+0.35}_{-0.36}$	–0.79 $^{+0.63}_{-0.17}$	–0.78 $^{+0.18}_{-0.26}$...
58	CXOU J043126.0–050639	04 31 26.07	–05 06 39.6	224.6	295.4	5.96±1.24	4.79	24.6	+0.61 $^{+0.36}_{-1.29}$	+0.74 $^{+0.24}_{-1.13}$	+0.24 $^{+0.26}_{-0.30}$	f
59	CXOU J043153.0–050659	04 31 53.06	–05 06 59.0	225.0	327.7	4.65±1.07	4.35	19.2	–0.51 $^{+0.27}_{-0.20}$	–0.78 $^{+0.30}_{-0.13}$	–0.46 $^{+0.50}_{-0.32}$	e,f
60	CXOU J043153.9–050656	04 31 53.90	–05 06 56.8	235.0	343.6	4.29±1.05	4.09	17.7	+0.69 $^{+0.30}_{-1.42}$	+0.76 $^{+0.24}_{-1.41}$	+0.13 $^{+0.30}_{-0.33}$...
61	CXOU J043131.2–050832	04 31 31.21	–05 08 32.6	240.0	252.8	2.40±0.84	2.86	9.9	+0.56 $^{+0.39}_{-1.07}$	–0.17 $^{+0.03}_{-0.76}$	–0.66 $^{+0.81}_{-0.28}$...
62	CXOU J043123.9–050546	04 31 23.95	–05 05 46.2	240.6	340.1	2.22±0.78	2.84	9.1	+1.00 $^{+0.00}_{-0.00}$	+1.00 $^{+0.00}_{-0.00}$	+0.11 $^{+0.44}_{-0.09}$...
63	CXOU J043126.5–050729	04 31 26.51	–05 07 29.7	243.4	297.4	3.62±1.00	3.62	14.9	–0.46 $^{+0.35}_{-0.71}$	–0.67 $^{+0.55}_{-0.06}$	–0.31 $^{+0.99}_{-0.31}$	d
64	CXOU J043155.4–050311	04 31 55.43	–05 03 11.5	261.2	335.9	6.25±1.27	4.92	25.7	–0.08 $^{+0.30}_{-0.29}$	–0.60 $^{+0.35}_{-0.21}$	–0.55 $^{+0.34}_{-0.22}$	f
65	CXOU J043155.9–050255	04 31 55.98	–05 02 55.1	276.2	350.1	6.53±1.31	5.00	26.9	–0.03 $^{+0.31}_{-0.31}$	–0.51 $^{+0.37}_{-0.25}$	–0.48 $^{+0.32}_{-0.23}$	f
66	CXOU J043124.2–050232	04 31 24.22	–05 02 32.3	282.3	405.2	0.82±0.47	1.76	3.4	+1.00 $^{+0.00}_{-2.00}$	+1.00 $^{+0.00}_{-2.00}$	–0.80 $^{+1.79}_{-0.20}$...
67	CXOU J043130.2–050918	04 31 30.29	–05 09 18.3	286.1	297.3	14.34±1.99	7.21	59.1	–0.12 $^{+0.19}_{-0.18}$	–0.67 $^{+0.23}_{-0.15}$	–0.60 $^{+0.24}_{-0.17}$	f
68	CXOU J043138.6–051011	04 31 38.65	–05 10 11.1	301.2	308.2	6.14±1.35	4.54	25.3	–0.45 $^{+0.27}_{-0.21}$	–0.64 $^{+0.29}_{-0.18}$	–0.27 $^{+0.41}_{-0.33}$	f
69	CXOU J043150.8–050953	04 31 50.83	–05 09 53.3	326.8	412.8	4.10±1.17	3.50	16.9	+0.51 $^{+1.22}_{-0.35}$	–0.65 $^{+1.63}_{-0.35}$	–0.87 $^{+1.09}_{-0.13}$...
70	CXOU J043127.7–051021	04 31 27.75	–05 10 21.0	359.5	373.9	43.34±3.52	12.32	178.6	+0.14 $^{+0.12}_{-0.12}$	–0.39 $^{+0.13}_{-0.12}$	–0.51 $^{+0.09}_{-0.08}$	f
71	CXOU J043157.3–051006	04 31 57.39	–05 10 06.5	395.1	533.9	13.61±3.63	3.91	56.1	+0.04 $^{+0.33}_{-0.34}$	–0.67 $^{+0.44}_{-0.22}$	–0.69 $^{+0.37}_{-0.19}$	c,e

NOTE. — The units for L_X are 10^{38} erg s $^{-1}$ in the 0.3–10 keV band.^a Sources near the center may be confused with nearby sources, making their positions, fluxes, and extents uncertain.^b Source is noticeably more extended than PSF.^c Source is at the edge of the S3 detector, and flux is uncertain due to large exposure correction.^d Possible optical counterpart.^e Source may be variable.^f Source is part of analysis sample.

TABLE 2
X-RAY SPECTRAL FITS OF NGC 1600

Row	Origin	Region	N_H (10^{20} cm $^{-2}$)	Hard Component			Soft Component (mekal)			Counts	χ^2/dof
				Model	kT_h or Γ (keV)	F_X^h (^a)	kT_s (keV)	Abund. (solar)	F_X^s (^a)		
1	Sources	Field	(4.86)	Bremss	$4.73^{+1.24}_{-0.89}$	2.78	1318	52.2/48=1.09
2	Sources	Field	0.48 [<6.32]	Bremss	$5.69^{+1.88}_{-1.17}$	2.75	1318	50.7/47=1.08
3 ^b	Sources	Field	(4.86)	Power	$1.76^{+0.10}_{-0.09}$	3.26	1318	52.4/48=1.09
4	Sources	Field	$8.62^{+7.60}_{-7.74}$	Power	$1.84^{+0.20}_{-0.18}$	3.35	1318	51.8/47=1.10
5	Sources	Field	(4.86)	Diskbb	$1.44^{[>0.00]}$	0.88	1318	50.5/46=1.10
			(4.86)	Power	$1.95^{+2.23}_{-0.46}$	2.10		
6 ^c	Unresolved	1 a_{eff}	(4.86)	$1.02^{+0.03}_{-0.03}$	$0.15^{+0.02}_{-0.02}$	4.95	3662	168.6/87=1.94
7 ^c	Unresolved	1 a_{eff}	(4.86)	Power	(1.76)	$2.29^{+0.47}_{-0.48}$	$0.95^{+0.03}_{-0.03}$	$0.27^{+0.11}_{-0.07}$	3.46	3662	110.0/86=1.27
8 ^c	Unresolved	1 a_{eff}	$7.57^{+7.12}_{-4.61}$	Power	(1.76)	$3.42^{+0.72}_{-0.73}$	$0.93^{+0.06}_{-0.06}$	$0.26^{+0.10}_{-0.06}$	3.74	3662	108.8/85=1.28
9 ^c	Unresolved	1 a_{eff}	(4.86)	Power	(1.76)	0.07 [<1.76]	$0.84^{+0.03}_{-0.04}$	1000 [>0.59]	1.70	3662	78.7/83=0.95
							$2.38^{+0.44}_{-0.74}$	$0.79^{+0.72}_{-0.37}$	3.25		
10 ^{c,d}	Unresolved	1 a_{eff}	(4.86)	Power	(1.76)	0.19 [<1.93]	$0.85^{+0.04}_{-0.04}$	$1.07^{+0.00}_{-0.00}$	2.04	3662	79.9/84=0.95
							$2.55^{+0.52}_{-0.86}$	$1.07^{+0.49}_{-1.00}$	3.25		
11 ^c	Unresolved	$a < 9''$	(4.86)	Power	(1.76)	$0.59^{+0.23}_{-0.23}$	$0.84^{+0.04}_{-0.04}$	$0.46^{+1.29}_{-0.22}$	1.04	1078	24.4/28=0.87
12 ^c	Unresolved	$9'' < a < 18''$	(4.86)	Power	(1.76)	$0.57^{+0.19}_{-0.20}$	$0.88^{+0.05}_{-0.04}$	$0.64^{+5.46}_{-0.33}$	0.89	1010	27.8/28=0.99
13 ^c	Unresolved	$18'' < a < 41''$	(4.86)	Power	(1.76)	$0.83^{+0.37}_{-0.41}$	$1.29^{+0.18}_{-0.13}$	$0.35^{+0.41}_{-0.16}$	0.90	981	45.4/36=1.26
14 ^c	Unresolved	$41'' < a < 69''$	(4.86)	Power	(1.76)	0.30 [<0.77]	$1.43^{+0.21}_{-0.16}$	$0.31^{+0.27}_{-0.14}$	1.20	939	51.2/42=1.22
15 ^c	Unresolved	$69'' < a < 98''$	(4.86)	Power	(1.76)	$1.52^{+0.24}_{-0.24}$	$1.48^{+0.24}_{-0.27}$	995.21 [>0.788]	0.41	976	48.7/54=0.90
16 ^c	Unresolved	$98'' < a < 126''$	(4.86)	Power	(1.76)	$0.74^{+0.60}_{-0.72}$	$1.62^{+0.19}_{-0.19}$	$0.86^{+8.62}_{-0.42}$	0.44	961	57.4/60=0.96
17 ^c	Unresolved	$126'' < a < 155''$	(4.86)	Power	(1.76)	$1.09^{+0.61}_{-0.70}$	$1.38^{+0.35}_{-0.22}$	$0.31^{+1.67}_{-0.19}$	0.71	978	78.6/71=1.11
18 ^c	Unresolved	$155'' < a < 180''$	(4.86)	Power	(1.76)	0.05 [<0.75]	$1.63^{+0.36}_{-0.28}$	$0.31^{+0.46}_{-0.17}$	1.11	778	76.3/65=1.17

^a Units are 10^{-13} erg cm $^{-2}$ s $^{-1}$ in 0.3–10 keV band.

^b The adopted best-fit model for this emission.

^c The energy range for this spectrum excludes 1.9 - 2.1 keV.

^d The abundances for this spectrum were tied together.